UC Irvine
Faculty Publications

Title
Global teleconnections in the oceanic phosphorus cycle: Patterns, paths, and timescales

Permalink

Journal

ISSN

Authors
Holzer, Mark
Primeau, Francois W

Publication Date
2013-04-01

DOI

Copyright Information

Peer reviewed

Global teleconnections in the oceanic phosphorus cycle: Patterns, paths, and timescales

Mark Holzer[1,3] and François W. Primeau[2]

[1]   Nutrient transport and productivity teleconnections with the Southern Ocean are diagnosed in a data-assimilated circulation model coupled to a jointly optimized simple phosphorus cycling model. The North Atlantic has the strongest extratropical teleconnections with the Southern Ocean: phosphate (PO_4) last utilized in the Southern Ocean sustains $29 \pm 6\%$ of the subpolar and $14 \pm 6\%$ of the subtropical, new production in the North Atlantic. A PO_4 path-density diagnostic shows that these teleconnections are mediated by thermocline paths and reveals that most paths to anywhere north of 40°S lie in the deep Pacific. Forcing nearly complete Southern-Ocean nutrient utilization increases the overall number of paths to anywhere north of 40°S, but reduces the number of paths from the Pacific to the North Atlantic by trapping nutrients in return paths to the Southern Ocean. At the same time, the mean export-to-uptake transit times to anywhere north of 40°S increase, while the mean transit times to the North Atlantic decrease. Correspondingly, the amount of North-Atlantic production sustained by Southern-Ocean export increases in spite of decreased total production in response to Southern-Ocean nutrient trapping. The distributions of export-to-uptake, export-to-surface, and surface-to-surface transit times are computed and summarized in terms of their mean transit times and their mean interior residence times. The combined particle and advective–diffusive transport of nutrients is characterized by broad, skewed transit-time distributions, which result in mean residence times much longer than the mean transit times, in turn much longer than the most probable transit times.

1.   Introduction

[2]   The global ocean circulation connects open-ocean eco-systems across the world oceans through the long-range transport of nutrients. The resulting teleconnections in biological productivity may be surprisingly large: the global modeling study by *Sarmiento et al.* [2004] suggested that up to three quarters of the biological production north of 30°S is due to the transport of preformed nutrients from the Southern Ocean. The importance of subantarctic mode waters (SAMWs) in supplying the subtropical and subpolar North Atlantic with nutrients was also born out in the data analysis of *Williams et al.* [2006], who emphasize the isopycnal transport in subsurface "nutrient streams" [*Pelegrí*

and Csanady, 1991; *Pelegrí et al.*, 1996; *Williams et al.*, 2011; *Guo et al.*, 2012]. The recent study by *Palter et al.* [2010] focused on the role of the Southern Ocean in returning nutrients from the deep ocean to the pycnocline. These authors use tracers to tag water, phosphate (PO_4), and dissolved organic PO_4 for a number of interior water masses to infer transport pathways. In particular, they estimate that SAMW fuels 33 to 75% of the export production between 30°S and 30°N, with the percentage depending on the chosen diapycnal diffusivity, wind stress, and parameterized eddy-compensating fluxes.

[3]   More broadly, evidence is accumulating that horizontal transport and nutrient streams are just as important as vertical processes in supplying nutrients to the euphotic zone to sustain export production in the North Atlantic [*Jenkins and Doney*, 2003; *Palter et al.*, 2005; *Palter and Lozier*, 2008]. While inversions of hydrographic data have produced estimates of the large-scale fluxes of nutrients [*Ganachaud and Wunsch*, 2002], and *Williams et al.* [2006] use Lagrangian particles in an isopycnal ocean model to infer nutrient pathways in the Atlantic, the quantitative path density of nutrients has not been explored. The paths accessed by the nutrients are distinct from those of water masses because of the interplay of fluid transport with biological production and the resulting particle export and remineralization of organic matter.

[1]Department of Applied Mathematics, School of Mathematics and Statistics, University of New South Wales, Australia.
[2]Department of Earth System Science, University of California, Irvine, California, USA.
[3]Department of Applied Physics and Applied Mathematics, Columbia University, New York, New York, USA.

Corresponding author: M. Holzer, Department of Applied Mathematics, School of Mathematics and Statistics, University of New South Wales, Sydney, NSW 2052, Australia. (mholzer@unsw.edu.au)

[4] In this paper, we use a simple global data-assimilated phosphorus cycling model (F. W. Primeau et al., Southern Ocean nutrient trapping and the efficiency of the biological pump, submitted to *Journal of Geophysical Research: Oceans*, 2012) to systematically establish global productivity teleconnections and to quantify the nutrient transport pathways and timescales that mediate the teleconnections with Southern-Ocean productivity. The pathways and timescales that couple the biological productivity of two regions are key for understanding how perturbations of the biology in one part of the ocean affect the global pelagic ecosystem.

[5] Motivated in part by the possibility of increasing Southern-Ocean nutrient utilization through artificial fertilization in an attempt to draw carbon dioxide out the atmosphere [see, e.g., *Boyd et al.*, 2007; *Oschlies et al.*, 2010] and to shed light on the transport mechanisms at play in the nutrient cycle, we also examine how productivity teleconnections change for highly idealized perturbations of the Southern-Ocean biology. The key questions addressed in our paper thus are:

[6] 1. What are the world oceans' productivity teleconnections? In particular, what percentage of the local biological uptake was last exported elsewhere? If the Southern-Ocean production is perturbed, how do these teleconnections change?

[7] 2. What are the nutrient pathways that mediate the teleconnections, and how do they change if the nutrient trapping of the Southern Ocean is enhanced by increasing Southern-Ocean nutrient utilization?

[8] 3. What are the timescales with which productivity teleconnections with the Southern Ocean are communicated across the world oceans?

[9] The data-assimilated phosphorus cycling model of Primeau et al. (submitted manuscript, 2012) (PHD, hereafter) is ideal for answering these questions because it is completely linear in the phosphorus concentration variables, which allows us to apply powerful Green-function methods to analyze the system. While a number of studies [*Gnanadesikan et al.*, 2002, 2004; *Marinov et al.*, 2008; *Palter et al.*, 2010] have demonstrated that nutrient and water transport in free-running ocean models is sensitive to the wind forcing, diapycnal diffusivity, and meso-scale eddy parameterization employed, we reduce biases due to these particular sensitivities by objectively optimizing both the circulation and phosphorus cycling model [*DeVries and Primeau*, 2011, PHD]: by minimizing the mismatch with the observed radiocarbon, PO_4, and chlorofluorocarbon (CFC-11) tracer fields, the data-assimilated model's transport is constrained over a broad range of spatial and temporal scales.

[10] From the outset, we wish to be clear, however, that the model cannot capture the ocean's phosphorus cycle with complete fidelity. The circulation is steady and driven by annual-mean climatology, the assimilated data carries uncertainties, and in regions of high eddy kinetic energy the optimized velocity may be inaccurate on small scales because it may need to compensate for an assumed constant background diffusivity. *DeVries and Primeau* [2011] estimate the uncertainties in large-scale integrated quantities, such as ventilation volumes and mean ages, due to uncertainties in the data itself to be 10% or less. On the small scales, the circulation model, formulated on a C-grid, suffers from purely numerical grid-scale oscillations, and biological production in waters less than two grid cells deep (i.e., shallower than the model's euphotic zone) is explicitly zeroed out [PHD] to avoid unphysical nutrient trapping in poorly resolved coastal regions. Our highly idealized representation of the marine ecosystem introduces additional model uncertainty: Biological production is parameterized as entirely PO_4 limited, with simple proportionality to the PO_4 concentration. Nevertheless, jointly data constraining both the PO_4 uptake rate and the circulation yields dynamically mutually consistent circulation, production, and tracer fields, providing some assurance that the analysis reported below likely captures the gross, annual-mean features of the real ocean's pelagic phosphorus cycle.

[11] The phosphorus cycling model explicitly carries dissolved organic phosphorus (DOP), which is continuously oxidized to PO_4. The two forms of phosphorus are thus represented by a two-component tracer variable, requiring Green functions with a 2×2 structure. These Green functions and their adjoints are used to partition PO_4 and DOP according to the times and places of last uptake and the times and places to next uptake. We furthermore partition PO_4 into its preformed and regenerated components, allowing us to build transport diagnostics that contain a wealth of quantitative information on the ocean's phosphorus cycle.

[12] We begin by summarizing the phosphorus cycling model of PHD in section 2, followed in section 3 by an exposition of our diagnostics that are then applied to an analysis of the global phosphorus cycle: In section 4, we quantify the productivity teleconnections in terms of the fraction of the production sustained by each of six regions covering the global ocean; in section 5, we use the time-integrated path density of PO_4 to quantify the transport paths that mediate the teleconnections with Southern-Ocean productivity, and in section 6, we quantify the bulk timescales that characterize the export-to-uptake, export-to-surface, and surface-to-surface paths of PO_4. The PO_4 paths and timescales are contrasted with those of newly ventilated water to highlight the role of the particle transport and the weighting of source and sink regions by the production field.

2. The Model

[13] The starting point for our phosphorus cycling model is a data-assimilated, steady circulation similar to that of *DeVries and Primeau* [2011], except that we have doubled the horizontal resolution to $2° \times 2°$, and additionally assimilated PO_4 and transiently evolving CFC-11. The CFC-11 adds important constraints for transport processes with decadal timescales to augment the information in the other tracer fields that are assimilated: natural radiocarbon, PO_4, temperature, and salinity. The model uses the wind-stress climatology of *Trenberth et al.* [1989] and has horizontal and vertical viscosities of $A_h = 5 \times 10^4 m^2 s^{-1}$ and $A_v = 10^{-4} m^2 s^{-1}$. The advective–diffusive transport operator has fixed horizontal and vertical eddy diffusivities of $10^3 m^2 s^{-1}$ and $10^{-5} m^2 s^{-1}$, respectively, typical of coarse-resolution models. The model uses linearized dynamics, with the missing higher-order terms represented by forcings that are adjustable control parameters in the optimization as described in detail by *DeVries and Primeau* [2011], but no explicit subgrid parameterizations

are employed. Additional control parameters that determine the model state, including the velocity field, are surface salinity and temperature, as well as the logarithm of the PO_4 uptake timescale field. During the assimilation process, these control parameters are continually adjusted to minimize an objective function that penalizes the mismatch with the observations not only for the dynamical variables, but also for the radiocarbon, PO_4, and CFC-11 tracer fields. The optimization essentially fits the model circulation and phosphorus cycle to the tracer data, and because the tracers encode the integrated effect of eddies and convection, the need for explicit subgrid parameterizations is avoided. The assimilation process thus results not only in an optimized circulation but also in an optimized PO_4 uptake field, which we use to build a completely linear phosphorus cycling model.

[14] The details of the optimization and model are described by PHD, who also compute the model's rigorously defined export production and quantify the quality of the model's tracer transport. Here we only summarize the salient features needed for developing the nutrient transport diagnostics presented below, but it is important to emphasize that with the jointly optimized circulation, particle-flux attenuation exponent (see below), and production field, the coupled circulation and phosphorus cycling model produces PO_4, natural radiocarbon, and CFC-11 fields that match the observational climatology closely [PHD]. Thus, while nutrient transport has been shown to be sensitive to the details of subgrid parameterizations in free-running ocean models [*Gnanadesikan et al.*, 2002, 2004; *Marinov et al.*, 2008; *Palter et al.*, 2010], we expect that our data-constrained model avoids much of the uncertainty due to these particular sensitivities. The model should therefore approximate the gross features of the real ocean's transport and pelagic phosphorus cycle to the extent that it suffices to use annual-mean steady flow and a simple linear uptake parameterization.

[15] Our diagnostic phosphorus cycling model is formulated in terms of the coupled PO_4/DOP system, and we denote the inorganic (subscript I) PO_4 concentration at location $\mathbf{r}$ by $P_I(\mathbf{r})$, and the organic (subscript O) DOP concentration by $P_O(\mathbf{r})$. (Notation and definitions developed throughout this paper are also collected in Appendix A.) We parameterize the biological production rate per unit volume, $J(\mathbf{r})$, also referred to as the uptake rate, as a loss rate of PO_4 in the euphotic layer that is proportional to the PO_4 concentration with rate constant $\gamma(\mathbf{r}) = J(\mathbf{r})/P_I(\mathbf{r})$. The euphotic layer is approximated as the top two layers of the model with a 73.4 m thickness. Below the euphotic layer $\gamma(\mathbf{r})$ is set to zero, ensuring $J(\mathbf{r}) = 0$ in the aphotic zone. The PO_4 taken up is instantly converted to DOP and vertically redistributed by a linear operator $\mathcal{S}$, which leaves a fraction $\sigma = 1/3$ of the DOP in the euphotic layer and distributes a fraction $1 - \sigma$ throughout the water column with a Martin-type power-law profile [*Martin et al.*, 1987]. The operator $\mathcal{S}$ acts on P_I to generate the vertically distributed amount of DOP that matches the loss of PO_4 due to uptake. The exponent of the power-law flux profile was jointly optimized along with $J(\mathbf{r})$ and the circulation and determined to be $b = 0.70$. The DOP then remineralizes with a constant rate coefficient κ, which we take as $\kappa = (0.5 \text{ years})^{-1}$. Details of the operator $\mathcal{S}$, as well as sensitivities of the equilibrium preformed and regenerated PO_4 fields to the biological model parameters κ, σ, and b may be found in PHD.

[16] For simplicity, we approximate both the circulation and the biology as steady so that all rate coefficients are time independent. The linear phosphorus cycling model may then be written as

$$\frac{\partial}{\partial t} \begin{bmatrix} P_I \\ P_O \end{bmatrix} + \begin{bmatrix} \mathcal{T} + \gamma & -\kappa \\ 0 & \mathcal{T} + \kappa \end{bmatrix} \begin{bmatrix} P_I \\ P_O \end{bmatrix} = \begin{bmatrix} 0 \\ \mathcal{S}P_I \end{bmatrix}, \quad (1)$$

where $\mathcal{T}$ is the linear advection–diffusion operator determined by the data assimilation. We may write equation (1) for the two component tracer $\mathbf{P} \equiv [P_I, P_O]^T$ more succinctly as

$$\partial_t \mathbf{P} + \mathbf{AP} = \mathbf{S}, \quad (2)$$

where $\mathbf{S} \equiv [0, S(\mathbf{r},t)]^T$, with $S(\mathbf{r}, t) = \mathcal{S}P_I$ being the source of DOP at $\mathbf{r}$ and time t.

[17] Note that equations (1) and (2) are linear in the PO_4 and DOP concentrations, which is not the case for conditional-restoring-type models [*Najjar et al.*, 1992] that parameterize uptake as a restoring of the surface PO_4 to observations only if the modeled concentrations exceed observations. The conditional nature of this restoring introduces a nonlinearity that is avoided here by having a fixed rate-constant field, $\gamma(\mathbf{r})$. Because of its complete linearity, model (1) can immediately be analyzed in terms of Green functions, which we exploit below to partition nutrients according to where they were last exported or last at the surface and where they will either again participate in production or where they will return to the surface layer (where, by definition, they are then part of the preformed pool). Green functions, and the closely related boundary propagators, have proven very useful in a number of studies for tracking geophysical fluids to and from specified regions [e.g., *Holzer and Hall*, 2000, 2008; *Primeau*, 2005; *DeVries and Primeau*, 2009] – here we extend their use to track not only fluid but also PO_4 and DOP.

3. The Diagnostic Equations

3.1. Green Function and Partitioned PO_4 and DOP

[18] In order to diagnose the nutrient transport, we consider the source on the right-hand side of equation (2) as prescribed. It is then natural to consider the standard Green function, $\mathbf{G}$ of equation (2), which is the response to a unit source for the coupled PO_4/DOP system at location $\mathbf{r}'$ and time t'. Because of the two-component nature of the system, $\mathbf{G}$ has a 2×2 structure of four components (the same structure as the phosphorus cycling operator $\mathbf{A}$ in equation (2)):

$$\mathbf{G} = \begin{bmatrix} G_{II} & G_{IO} \\ G_{OI} & G_{OO} \end{bmatrix}, \quad (3)$$

where G_{II} represents the PO_4 response to a unit (inorganic) PO_4 source, G_{IO} the PO_4 response to a unit DOP source, G_{OI} the DOP response to a unit PO_4 source, and G_{OO} the DOP response to a unit DOP source. Because PO_4 is only converted to DOP by the prescribed source, we have $G_{OI} \equiv 0$. The Green function of equation (1) thus obeys

$$\frac{\partial}{\partial t} \mathbf{G}(\mathbf{r}, t | \mathbf{r}', t') + \mathbf{AG}(\mathbf{r}, t | \mathbf{r}', t') = \mathbf{I}\delta(\mathbf{r} - \mathbf{r}')\delta(t - t'), \quad (4)$$

where $\mathbf{I}$ is the 2×2 identity matrix. Equation (4) is subject to zero-flux boundary conditions because all sources and

sinks are considered interior to the domain. (We revisit the issue of boundary conditions in section 6, when we partition the nutrient field into its preformed and regenerated components.) For an arbitrary source and initial condition, the solution of the PO_4/DOP system can be expressed as a source-weighted superposition of unit point-source responses, that is, as a convolution of **G** and **S** over source location **r′** and source time $t′$.

[19] Because our model cycles all biological production, including particulate organic phosphorus, into DOP before having it eventually remineralize into PO_4, we consider only DOP sources. For computational efficiency, we do not consider the response to a point source at $(\mathbf{r}′, t′)$, but instead the response to $S(\mathbf{r}′, t′)$ integrated over a finite region. To this end, we divide the euphotic layer into nonoverlapping regions Ω_i, which define masks such that $\Omega_i(\mathbf{r}′, t′) = 1$ if $\mathbf{r}′$ is in the region and $\Omega_i = 0$ otherwise.

[20] The production that occurs in region $\Omega_i(\mathbf{r}′, t_i)$ during the interval $(t_i, t_i + dt_i)$ is given by $S(\mathbf{r}′, t_i)\Omega_i(\mathbf{r}′, t_i)dt_i$, and this production makes the contributions

$$g_X^{\downarrow}(\mathbf{r}, t|\Omega_i, t_i)dt_i \equiv dt_i \int d^3r′ \, G_{XO}(\mathbf{r}, t|\mathbf{r}′, t_i)S(\mathbf{r}′, t_i)\Omega_i(\mathbf{r}′, t_i), \quad (5)$$

to the PO_4 (subscript $X=I$) and DOP (subscript $X=O$) mass per unit volume at $(\mathbf{r},t)$. (In equation (5), $d^3r′$ is the volume element with respect to $\mathbf{r}′$ and the integral is over the entire ocean volume, with the Ω_i mask selecting the source region of interest.) The downward arrow superscript on $g_X^{\downarrow}$ indicates that $g_X^{\downarrow}$ pertains to the "in" (Ω_i DOP source to point $\mathbf{r}$) part of the transport problem (Figure 1). For our steady model, both the masks Ω_i and the production source S are time independent, but in general they need not be as our notation indicates.

[21] The local fractions of the PO_4 or DOP at $(\mathbf{r},t)$ that were last utilized in Ω_i during $(t_i, t_i + dt_i)$ are then given by

$$\mathcal{G}_X(\mathbf{r}, t|\Omega_i, t_i)dt_i \equiv \frac{g_X^{\downarrow}(\mathbf{r}, t|\Omega_i, t_i)dt_i}{P_X(\mathbf{r}, t)}. \quad (6)$$

In equation (6) the quantity $\mathcal{G}_X$ is a density per unit t_i time that can be interpreted as a probability density function with
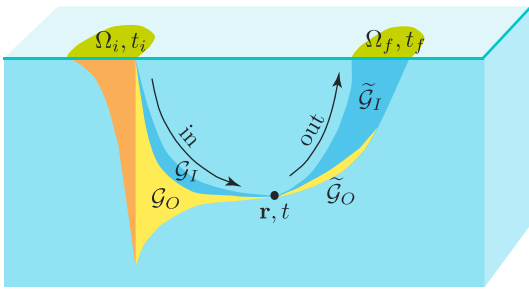

Figure 1. Schematic of the phosphate and DOP partitioning at location **r** and time t. The quantities $\mathcal{G}_I dt_i$ and $\mathcal{G}_O dt_i$ are the local fractions of phosphate and DOP that were last produced in region Ω_i during $(t_i, t_i + dt_i)$, and $\widetilde{\mathcal{G}}_I dt_f$ and $\widetilde{\mathcal{G}}_O dt_f$ are the local fractions of phosphate and DOP that will next be taken up in region Ω_f during $(t_f, t_f + dt_f)$ (once the DOP has remineralized). Colors indicate DOP in yellow and phosphate in dark blue; green indicates biological production, and brown, the particulate plume with a Martin-type power-law attenuation in the vertical. Detailed definitions are provided in the text.

respect to t_i. The distribution $\mathcal{G}_X$ is analogous to the boundary-propagator Green function [*Holzer and Hall*, 2000; *Primeau*, 2005].

[22] The local concentrations of PO_4 and DOP that will next be utilized ("taken up" biologically) in region Ω_f during the interval $(t_f, t_f + dt_f)$ are given by

$$g_X^{\uparrow}(\mathbf{r}, t|\Omega_f, t_f)dt_f \equiv dt_f \int d^3r′ \Omega_f(\mathbf{r}′, t_f)\gamma(\mathbf{r}′, t_f)G_{IX}(\mathbf{r}′, t_f|\mathbf{r}, t)P_X(\mathbf{r}, t).$$
$$(7)$$

The upward arrow superscript indicates that $g_X^{\uparrow}$ pertains to the "out" (point $\mathbf{r}$ to Ω_f uptake) part of the transport problem (Figure 1). The local fractions of the total PO_4 and DOP at $(\mathbf{r},t)$ that will be taken up in Ω_f during $(t_f, t_f + dt_f)$ are thus given by

$$\widetilde{\mathcal{G}}_X(\mathbf{r}, t|\Omega_f, t_f)dt_f \equiv \frac{g_X^{\uparrow}(\mathbf{r}, t|\Omega_f, t_f)dt_f}{P_X(\mathbf{r}, t)} \quad (8)$$

$$= \int d^3r′ \Omega_f(\mathbf{r}′, t_f)\gamma(\mathbf{r}′, t_f)G_{IX}(\mathbf{r}′, t_f|\mathbf{r}, t). \quad (9)$$

[23] Note that G_X and $\widetilde{G}_X$ simply partition PO_4 and DOP at an interior point according to the locations and times either since last uptake ($\mathcal{G}$'s) or to next uptake ($\widetilde{\mathcal{G}}$'s). The distributions $\mathcal{G}_X$ and $\widetilde{\mathcal{G}}_X$ are, therefore, joint distributions with respect to (Ω_i, t_i) and (Ω_f, t_f), respectively, with the normalizations

$$\sum_{\Omega_i} \int_{-\infty}^{t} dt_i \, \mathcal{G}_X(\mathbf{r}, t|\Omega_i, t_i) = 1 \quad \text{and} \quad (10)$$

$$\sum_{\Omega_f} \int_{t}^{\infty} dt_f \, \widetilde{\mathcal{G}}_X(\mathbf{r}, t|\Omega_f, t_f) = 1,$$

where we assumed adjacent, nonoverlapping sets of masks, Ω_i and Ω_f, with each set summing to a single mask for the global euphotic zone.

[24] As shown in Appendix B, it is much more efficient to compute the distributions $\mathcal{G}_X$ and $\widetilde{\mathcal{G}}_X$ directly without computing the full point-to-point Green function **G**. To compute $\widetilde{\mathcal{G}}$, whose source and field arguments are flipped from those for $\mathcal{G}$, we use the reciprocity of the fundamental Green function $\mathbf{G}^{\dagger}(\mathbf{r}, t|\mathbf{r}′, t′) = \mathbf{G}^T(\mathbf{r}′, t′|\mathbf{r}, t)$ to perform the calculation in the time-reversed adjoint flow (see Appendix B). This allows both $\mathcal{G}$ and $\widetilde{\mathcal{G}}$ to be computed as single tracer fields for each Ω_i or Ω_f. The distributions $\mathcal{G}_X$ contain complete information on transport since last uptake, while the distributions $\widetilde{\mathcal{G}}_X$ contain complete information on transport to next uptake.

[25] The source-time integrated distributions have the following interpretations:

$$f_X^{\downarrow}(\mathbf{r}, t|\Omega_i) = \int_{-\infty}^{t} dt_i \, \mathcal{G}_X(\mathbf{r}, t|\Omega_i, t_i) \quad (11)$$

is the fraction of PO_4 or DOP at $(\mathbf{r},t)$ last produced in region Ω_i regardless of when the production occurred, and

$$f_X^{\uparrow}(\mathbf{r}, t|\Omega_f) = \int_{t}^{\infty} dt_f \, \widetilde{\mathcal{G}}_X(\mathbf{r}, t|\Omega_f, t_f) \quad (12)$$

is the fraction of PO_4 or DOP at $(\mathbf{r},t)$ that will next be taken up in region Ω_f regardless of when the uptake will occur.

The arrow superscripts again indicate whether the fractions pertain to the "in" (downward arrow) or "out" (upward arrow) part of the transport problem. For the steady-flow case considered here, we compute these fractions by directly solving the discretized equations for the time-integrated nutrient portions $g_X^{\downarrow}$ and $g_X^{\uparrow}/P_X$ defined in equations (5) and (9) via direct matrix inversion (see Appendix B for details).
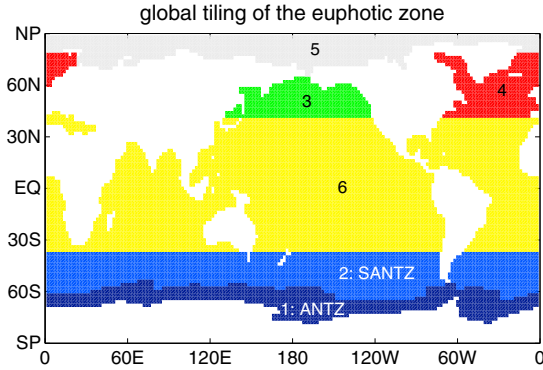

Figure 2. The global tiling of the euphotic zone into the six regions considered in this study. The division of the ocean south of 40°S into an Antarctic zone (ANTZ) and a subantarctic zone (SANTZ) is based on the latitude of maximum Ekman divergence.

4. Teleconnection Patterns

[26] To quantify and understand how the interplay between export production and the ocean circulation couples biological productivity across the world oceans, we begin by asking where the nutrients sustaining local production were last utilized. To identify the region of last utilization, we subdivide the global ocean surface into the six regions shown in Figure 2. The ocean south of 40°S is subdivided into an Antarctic zone (ANTZ) and a subantarctic zone (SANTZ), based on the latitude of the maximum Ekman divergence. Surface waters of the ANTZ are destined to primarily sink as AABW, while surface waters of the SANTZ are primarily transported north to be eventually subducted as Antarctic intermediate water and SAMW.

4.1. Teleconnections in the Base Equilibrium

[27] We will refer to the fraction of the local production sustained by nutrients last utilized in a given region as the "production fraction from that region." Because of the simplicity of our uptake parameterization, namely $J(\mathbf{r}) = \gamma(\mathbf{r})P_I(\mathbf{r})$ with prescribed rate coefficients, $\gamma(\mathbf{r})$, the fraction of the production at $\mathbf{r}$ in the euphotic zone that is sustained by nutrients last utilized in a given region Ω_i is simply the fraction $f_I^{\downarrow}(\mathbf{r}|\Omega_i)$ of the PO$_4$ last utilized in Ω_i, which is readily computed for our steady model as shown in Appendix B.

[28] The zonally averaged production and its production fractions from each of the six regions tiling the global ocean surface (Figure 2) are plotted in Figure 3 for the data-assimilated,
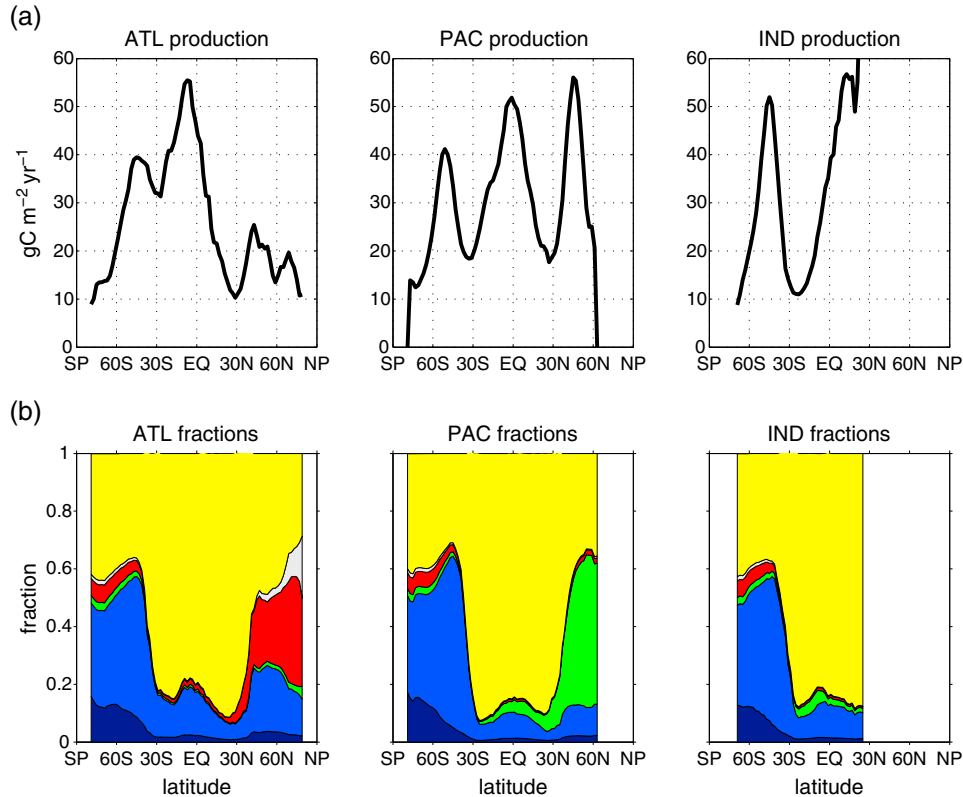

Figure 3. (a) The production rate per unit area zonally averaged in each basin for the data-assimilated (unperturbed) equilibrium phosphorus cycle. (b) The corresponding zonally averaged fraction of production sustained by nutrients last exported in each of the six color-coded regions tiling the global euphotic zone defined in Figure 2.

unperturbed phosphorus cycle (the "base equilibrium"). The zonally averaged production (Figure 3a) shows minima in the subtropical gyres of each basin, as expected for regions of large-scale downwelling. Production maxima occur in the Southern Ocean and in equatorial upwelling regions. The Pacific also has high production at the southern edge of the North-Pacific subpolar gyre. In the North Atlantic, the subpolar maximum is less than half that of the Pacific, but regions of high productivity extend into the Arctic Ocean.

[29] The production fractions of Figure 3b define and quantify the phosphorus cycle's global teleconnection patterns. The plotted production fractions are volume-weighted vertical averages over the model's euphotic zone (top two layers) that are zonally averaged for each basin. The production fractions show that up to ~27% of the production in the midlatitude and subpolar North Atlantic are sustained by nutrients last utilized in the Southern Ocean, with the bulk of these nutrients (~23%) coming from the SANTZ. The dominance of SANTZ over ANTZ in the teleconnection pattern is consistent with the concept of a biogeochemical divide [PHD and *Marinov et al.*, 2006]. In the North Atlantic, the production sustained by nutrients last taken up in the Southern-Ocean (blues) is comparable to the production sustained by nutrients that are regionally recycled in the North Atlantic (about 25–35%), with the bulk of the remainder being sustained by equatorial and subtropical export (yellow). In the subpolar North Atlantic (30–60°N), the production fractions from the Arctic and North Pacific are small (each contributes just a few percent). For the Pacific and Indian Oceans, the production fraction from the Southern Ocean is roughly 10%. For the Pacific north of ~45 °N, regional recycling of North Pacific nutrients (green) dominates production, while for the Indian Ocean, nutrients last exported in equatorial and subtropical regions (yellow) dominate. It is also interesting to note that ~40% of the production in the Southern Ocean is sustained by nutrients last taken up between 40°S and 40°N (yellow band). This shows that in the base equilibrium, there is only partial nutrient trapping in the Southern Ocean, with a significant fraction of the nutrients sustaining Southern-Ocean production being transported from low latitudes, where the bulk of the global production occurs. Our path-density diagnostic (developed below) shows that the dominant pathway from low latitudes (which is not the focus of this study) is via deep waters that then upwell and are mixed to the euphotic zone in the Southern Ocean.

[30] To quantify the horizontal structure of the productivity teleconnections with the Southern Ocean, Figure 4 shows a map of the euphotic-zone averaged fraction of the new production [*Gnanadesikan et al.*, 2002], $J_{new} \equiv J - \kappa P_O$, sustained by nutrients last exported in the Southern Ocean (defined as the union SANTZ ∪ ANTZ, which is the ocean south of 40°S). This fraction is computed as $\gamma(\mathbf{r})f_I^\downarrow(\mathbf{r}|\Omega_i)P_I(\mathbf{r})/J_{new}(\mathbf{r})$ with $\Omega_i = $ SANTZ ∪ ANTZ. The production sustained by the SANTZ is the main contributor to this fraction. The fraction sustained by the ANTZ has a similar pattern, but is reduced in amplitude by roughly an order of magnitude. We express the fraction here in terms of J_{new}, rather than J itself, to give a better idea about the remote fertilization of the local production that is actually exported, rather than recycled within the euphotic zone.
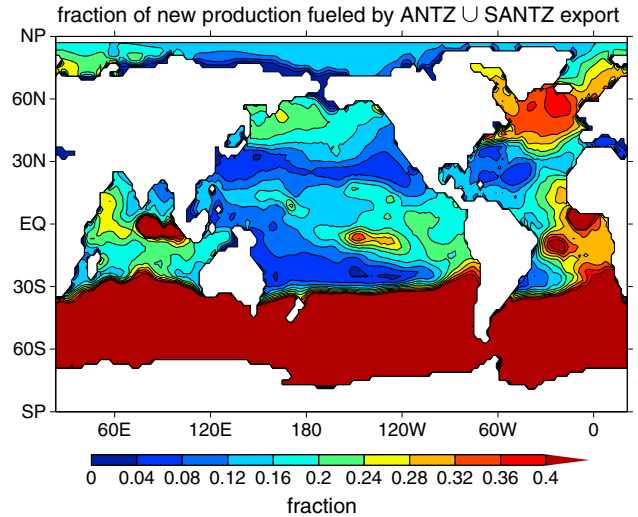

fraction of new production fueled by ANTZ ∪ SANTZ export

Figure 4. The fraction of the local new production, defined as $\gamma P_I - \kappa P_O$ for the euphotic zone, sustained by nutrients last utilized south of 40°S. This fraction has been vertically volume averaged over the euphotic zone and horizontally smoothed with two passes of an area-weighted nearest neighbor average to remove grid-scale noise.

Because the recycling within the euphotic zone is not strongly constrained by assimilating PO_4, the fraction of J_{new} is likely also a more robust measure of the teleconnections. The high fractions seen in divergent equatorial upwelling regions, particularly in the eastern Atlantic and Indian Ocean, are due to the fact that in these regions, there is significant remineralization of DOP within the euphotic zone so that J_{new} is significantly smaller than J there (~30% zonally averaged). Away from the equatorial regions, the map is dominated by the teleconnection with the North-Atlantic subpolar gyre, a region that has access to nutrient-rich deep waters through Ekman suction and localized vertical mixing. An important nutrient supply mechanism for the subpolar gyre is a subsurface nutrient stream that has been shown to supply the North-Atlantic subpolar gyre via isopycnal transport into the deep winter mixed layer, where convection brings the nutrients to the euphotic zone [*Williams et al.*, 2006]. While poorly resolved in our model, the signature of the Gulf-stream nutrient stream is visible in Figure 4, and a similar, but weaker, feature can also be seen in the southern part of the Pacific subpolar gyre, where the Kuroshio current is also associated with a nutrient stream [*Guo et al.*, 2012].

[31] Because the dominant teleconnection in the Northern Hemisphere is with the subpolar North Atlantic, and because there is a longstanding interest in how export production in the oligotrophic subtropical North Atlantic is sustained [e.g., *Jenkins*, 1982; *McGillicuddy et al.*, 2003; *Jenkins and Doney*, 2003; *Palter et al.*, 2005], we will from now on primarily focus on the productivity teleconnections with the North Atlantic. To that end, we define the subpolar and subtropical North-Atlantic regions (SubPlrNA and SubTroNA), shown in Figure 5. The SubTroNA region is based on where the optimized production falls below 18 gC m^{-2} yr^{-1}, and the roughly three times smaller SubPlrNA region is simply the North Atlantic north of SubTroNA. The teleconnections with the Southern Ocean in terms of the region-integrated
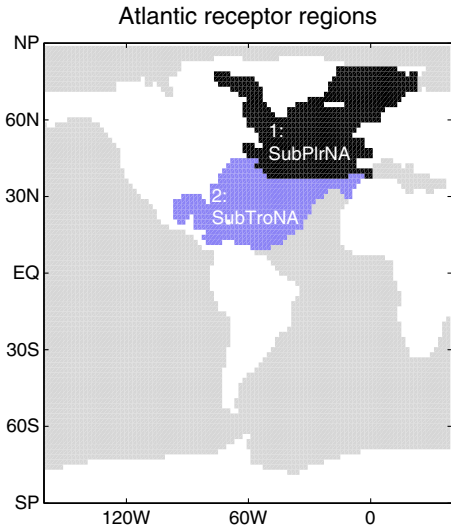
Figure 5. The subpolar and subtropical North-Atlantic receptor regions, SubPlrNA and SubTroNA, considered in this study. These regions are based approximately on the (unperturbed) data-assimilated equilibrium production field. The subtropical region is defined as the part of the North Atlantic where production falls everywhere below 18 gC m^{-2} yr^{-1}. The SubTroNA has an area of 6.2×10^{13} m^2 sustaining an average new production of 1.9 gC m^{-2} yr^{-1}, while the SubPlrNA has an area of 2.0×10^{13} m^2 with an average new production of 12 gC m^{-2} yr^{-1}, using a C:P ratio of 106:1.

new production are $29 \pm 6\%$ for the SubPlrNA and $14 \pm 6\%$ for the SubTroNA, where the uncertainties are due to the plausible ranges of the phosphorus cycling model parameters, b, σ, and κ (Appendix C).

4.2. Teleconnections With Increased Southern-Ocean Nutrient Utilization

[32] We now ask how the productivity teleconnections of the equilibrium phosphorus cycle change when Southern-Ocean production is perturbed. While in PHD we perturbed production by scaling $\gamma(\mathbf{r})$ by a constant factor over the perturbation region, here we simply set $\gamma(\mathbf{r})$ to a spatially uniform value of $1/\tau_B$ over the region. The main reason for using absolute, spatially uniform perturbations here is to provide a stronger perturbation in areas where the base-state $\gamma(\mathbf{r})$ is very small, such as near Antarctica and around the tip of South America. With the absolute perturbations, and a sufficiently small τ_B, we achieve nearly complete, spatially uniform nutrient utilization.

[33] While it is clear that $\tau_B = 0$ will give a maximum response, an infinite uptake rate is singular and we seek the largest value of τ_B for which the response is still saturated at the $\tau_B = 0$ asymptotic level. For reference, the base-state $\gamma(\mathbf{r})$ averaged over the ocean south of 40°S gives $\bar{\gamma}_{SO} = (3.5 \text{ years})^{-1}$. To determine a finite value for τ_B with which to perturb the Southern Ocean in order to get a maximum production response in the North Atlantic, we plot in Figure 6 the SubPlrNA and SubTroNA integrated production as a function of τ_B, for the cases where γ is set to $1/\tau_B$ over SANTZ, ANTZ, and SANTZ $\cup$ ANTZ.

[34] Figure 6 shows that increasing production in the Southern Ocean (decreasing τ_B) decreases production in
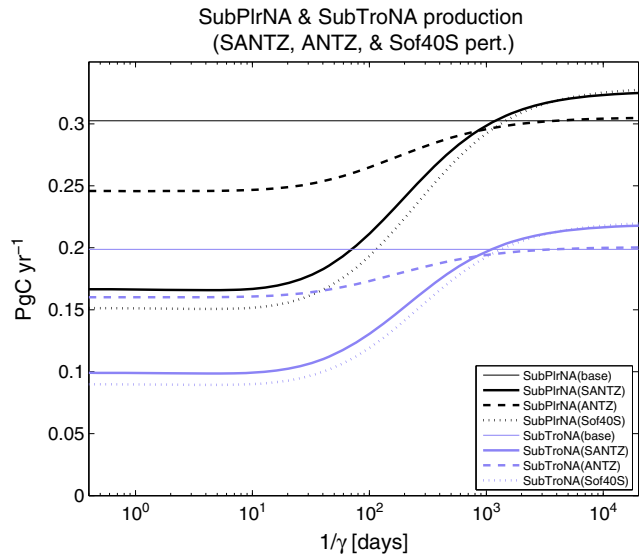

Figure 6. The equilibrium production rate integrated over the subpolar (black curves) and subtropical (purple curves) North-Atlantic receptor regions of Figure 5 for uptake perturbations where $1/\gamma$ is set to the value of the abscissa spatially uniform over the perturbation region indicated by the line style: SANTZ (thick solid), ANTZ (dashed), SANTZ $\cup$ ANTZ (dotted). The thin horizontal lines indicate the unperturbed base equilibrium production rate of the two receptor regions. The union SANTZ $\cup$ ANTZ is simply the ocean south of 40°S.

the North Atlantic. The reason is nutrient trapping in the Southern Ocean as discussed in PHD and further quantified in section 5. As τ_B is reduced, the North-Atlantic production decrease saturates at $\tau_B \simeq 10$ days. Consistent with the idea of a biogeochemical divide, perturbing the SANTZ has a much larger effect on North-Atlantic productivity than perturbing the ANTZ. (The reverse is true for the efficiency of the biological pump [PHD, *Marinov et al.*, 2006].) For large values of τ_B over the ANTZ (negligible ANTZ production), the production in the North Atlantic is hardly changed from its unperturbed values, underscoring the unimportance of ANTZ export to global productivity teleconnections in the present biogeochemical state of the ocean. This is also evident from the fact that perturbing the SANTZ $\cup$ ANTZ does not lead to a much larger response than only perturbing the SANTZ. While our phosphorus cycling model is linear in the concentrations, perturbing γ represents a nonlinear change to the nutrient cycle. This nonlinearity is manifest in the fact that the difference between the responses to SANTZ and SANTZ $\cup$ ANTZ perturbations is much smaller than the response to perturbing the ANTZ only. Because the SANTZ is the region most strongly teleconnected to the North Atlantic, we now investigate the effect of the idealized perturbation of setting $\gamma = (10 \text{ days})^{-1}$ over SANTZ to achieve the maximum response. With $\gamma = (10 \text{ days})^{-1}$ over the SANTZ, the SANTZ averaged surface PO$_4$ concentration is reduced by a factor of $\sim$20 and thus nearly depleted.

[35] Figure 7a summarizes the remote production response to increased SANTZ nutrient utilization with $\gamma = (10 \text{ days})^{-1}$. To first order, the pattern of the zonally averaged production north of 40°S is preserved but reduced in amplitude (see also
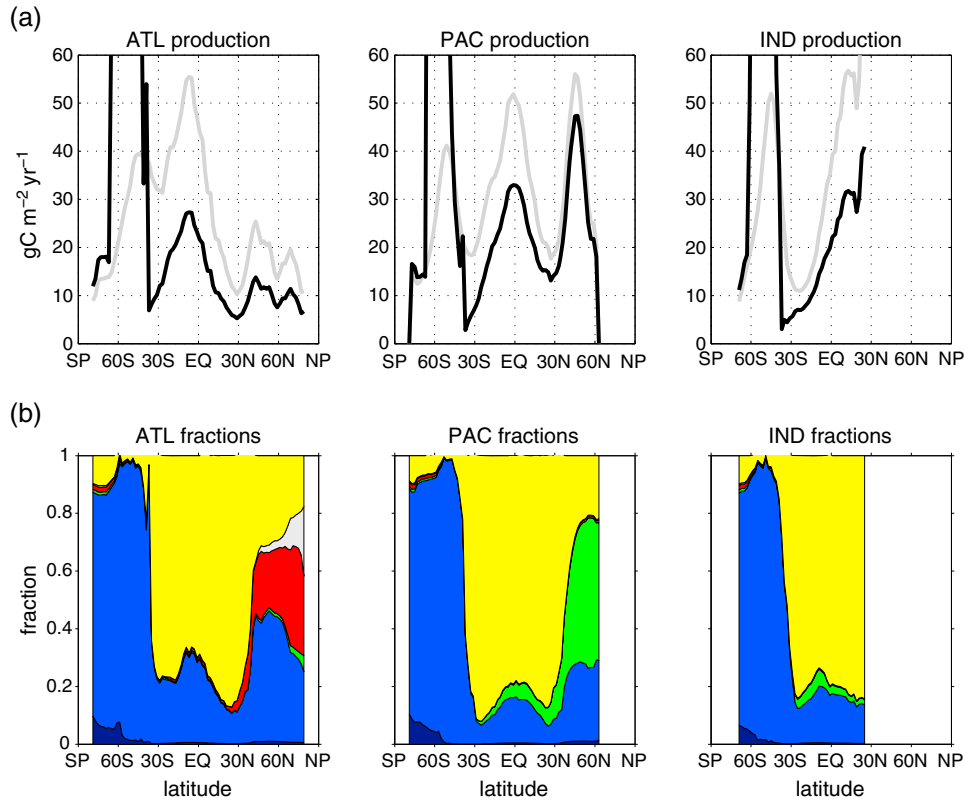
Figure 7. (a) The production rate per unit area, zonally averaged for each basin. The black curves show the production in the perturbed state for which the SANTZ uptake rate is prescribed to be $\gamma = (10\ \text{days})^{-1}$. The gray curves show the production rate for the data-assimilated base equilibrium state (same as in Figure 3) for reference. (b) The zonally averaged fraction of production in the perturbed state that is sustained by nutrients last exported in each of the six color-coded regions tiling the global euphotic zone defined in Figure 2.

PHD). With strongly increased SANTZ export production, we expect a greater proportion of nutrients last utilized in the SANTZ to sustain production in the rest of the world ocean, particularly in the NH. This is clearly evident in Figure 7b, which shows the corresponding production fractions. Compared to the base state (Figure 3b), the zonally averaged fraction sustained by Southern-Ocean nutrients is increased by a factor of roughly 1.5 to 2 in all basins. For all basins, the SANTZ fraction increases primarily at the expense of the equatorial and subtropical fraction (yellow). The regionally recycled fractions in the North Atlantic (red in the ATL panel) and Pacific (green in the PAC panel) do not change much.

[36] To highlight the changes in the North Atlantic, where the teleconnections with the Southern Ocean are strongest, Figure 8 shows the Atlantic-basin zonally averaged differences between the SANTZ-nutrient-drawdown and base equilibrium states. For latitudes 40 to 70°N, production drops by ~45% but the SANTZ production fraction increases by ~0.22 (from ~0.23 in the base state to ~0.45 in the perturbed state). For these latitudes, the production fractions from all other source regions, including ANTZ, are correspondingly reduced, with the bulk of the compensation being due to the equatorial and subtropical fraction (yellow). (The changes in the production fractions summed over all source regions must give zero, because the fractions always sum to unity.)

[37] Having quantified the degree to which Southern-Ocean export production is teleconnected to biological
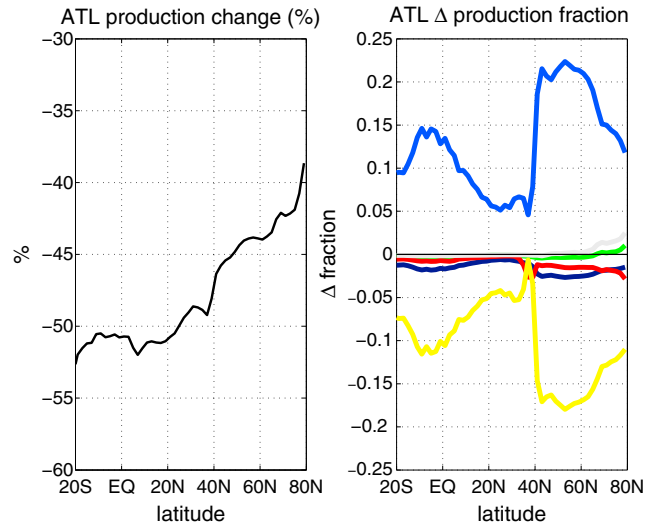
Figure 8. (a) The change in the zonally averaged production rate per unit area in the Atlantic north of 20°S in response to setting the biological uptake rate over the SANTZ to a spatially uniform $\gamma = (10\ \text{days})^{-1}$. (b) The corresponding changes in the Atlantic-basin zonally averaged fraction of production sustained by nutrients last exported in each of the six color-coded regions tiling the global euphotic zone defined in Figure 2. Note that these changes sum to zero because the fractions sum to unity.

uptake elsewhere in the world oceans, we now ask what the PO_4 transport paths are that mediate these teleconnections, what their equilibrium response to increased Southern-Ocean nutrient utilization is, and how the nutrient paths differ from the paths of water itself.

5. Nutrient Path Densities

5.1. The Path-density Diagnostic

[38] Here we quantify the export-to-uptake nutrient transport paths that operate in the base and perturbed equilibrium phosphorus cycles. Before defining the path density of PO_4, it is useful to consider the path density η_ρ of water itself [*Holzer and Primeau*, 2006, 2008]. We only consider residence-time integrated path densities $\bar{\eta}$ for steady flow in this paper, that is, the density of paths regardless of the transit time along the paths. The density $\bar{\eta}_\rho$ of water paths from surface region Ω_i to region Ω_f is then simply the local fraction of water that was last in contact with the surface in Ω_i and that will make next surface contact in Ω_f. This fraction is given by the product of the water-mass fraction $f_\rho^\downarrow(\mathbf{r}|\Omega_i)$ that was last in contact with Ω_i and the water-mass fraction $f_\rho^\uparrow(\mathbf{r}|\Omega_f)$ that will make next surface contact with Ω_f:

$$\bar{\eta}_\rho(\mathbf{r}, \Omega_i \to \Omega_f) = \rho f_\rho^\downarrow(\mathbf{r}|\Omega_i) f_\rho^\uparrow(\mathbf{r}|\Omega_f) \quad , \quad (13)$$

where we additionally multiply by the water density ρ, so that $\bar{\eta}_\rho$ has the interpretation of being the local mass density of water that is in $\Omega_i \to \Omega_f$ transit, with the normalization

$$\sum_{\Omega_i} \sum_{\Omega_f} \bar{\eta}_\rho(\mathbf{r}, \Omega_i \to \Omega_f) = \rho. \quad (14)$$

(This definition differs slightly from that of *Holzer and Primeau* [2006, 2008], where we additionally divided by the mass of the ocean to normalize the global volume integral of the path density.) Because every fluid element of the $\Omega_i \to \Omega_f$ density $\bar{\eta}_\rho$ traces out an advective–diffusive path from Ω_i to Ω_f, $\bar{\eta}_\rho$ is also the density of these $\Omega_i \to \Omega_f$ paths.

[39] The residence-time independent path density for PO_4, $\bar{\eta}_I$, is a straightforward generalization:

$$\bar{\eta}_I(\mathbf{r}, \Omega_i \to \Omega_f) = P_I(\mathbf{r}) f_I^\downarrow(\mathbf{r}|\Omega_i) f_I^\uparrow(\mathbf{r}|\Omega_f), \quad (15)$$

where $f_I^\downarrow(\mathbf{r}|\Omega_i)$ is the fraction of PO_4 at $\mathbf{r}$ last taken up in region Ω_i and $f_I^\uparrow(\mathbf{r}|\Omega_f)$ is the fraction of PO_4 at $\mathbf{r}$ that will next be taken up in region Ω_f, as defined by equations (11) and (12). The PO_4 path density has the normalization

$$\sum_{\Omega_i} \sum_{\Omega_f} \bar{\eta}_I(\mathbf{r}, \Omega_i \to \Omega_f) = P_I(\mathbf{r}, t). \quad (16)$$

Thus, $\bar{\eta}_I$ is simply the local concentration of PO_4 that is in transit from being last utilized in Ω_i to its next biological uptake in Ω_f. Because each PO_4 molecule of the $\Omega_i \to \Omega_f$ concentration $\bar{\eta}_I$ traces out a path from Ω_i to Ω_f that is governed by particle transport, advection, and eddy diffusion, $\bar{\eta}_I$ is also the density of these $\Omega_i \to \Omega_f$ PO_4 paths.

[40] We now consider the densities of paths beginning in the SANTZ for the base equilibrium state and for the perturbed equilibrium state in which the SANTZ nutrient utilization rate constant has been dramatically increased to a spatially uniform value of $\gamma = (10 \text{ days})^{-1}$. Vertical integrals

of the path densities (Figure 9) show that the PO_4 paths from the SANTZ to the North Atlantic are primarily concentrated in the Atlantic, while paths from SANTZ to anywhere north of 40°S (Nof40S) are primarily concentrated in the Pacific. To quantify the paths mediating the export-to-uptake teleconnections, we therefore consider the zonally averaged SANTZ→SubTroNA and SANTZ→SubPlrNA path densities in the Atlantic (Figure 10) and the zonally averaged SANTZ→SubPlrNA and SANTZ→Nof40S path densities in the Pacific (Figure 11). To quantify the Southern-Ocean nutrient trapping, we consider the path densities for the SANTZ→SANTZ return trip in both the Atlantic and Pacific.

5.2. The Path Densities of Water

[41] The densities of water paths from the SANTZ to key destination regions are shown in the first column of Figures 9–11. In both the Atlantic and Pacific, these water paths are largely confined to the thermocline. Water undergoing a SANTZ→SANTZ round trip barely reaches the Northern Hemisphere and is largely localized beneath the SANTZ. In the Atlantic, water destined for the SubTroNA and water destined for the SubPlrNA (Figure 10) are similarly organized with the highest path densities in the tropics and subtropics. However, there are roughly five times more water paths to the SubPlrNA than to the SubTroNA, as expected because the SubPlrNA is characterized by large-scale downwelling. In the Pacific (Figure 11), there is ∼30 times less water undergoing the SANTZ→SubTroNA journey than in the Atlantic, and this water is organized into the Antarctic Circumpolar Current (ACC) and bleeds out northward with the mode waters. Water starting at the SANTZ surface that is headed to anywhere north of 40°S is primarily found in the Pacific (Figure 9). The Pacific-sector zonally averaged SANTZ→Nof40S path density (Figure 11) shows that these paths lead primarily to equatorial upwelling and reach deeper with increasing latitude, consistent with the water-mass analysis of *Khatiwala et al.* [2012].

[42] The paths connecting the SANTZ to the North Atlantic (Figure 10) tend to have a low density near their origin and destination regions and a high density in between. This is a generic feature of the path-density diagnostic [*Holzer and Primeau*, 2006, 2008; *Holzer*, 2009]: The path density identifies the local amount of origin-labeled water that is destined for the destination region. Close to the source and destination regions, eddy-diffusive transport produces an overwhelming number of source-to-source and destination-to-destination paths that dilute the long-range paths immediately after they leave the source and as they approach the destination. (For purely advective flow along a single "conveyor" path, the path density would be constant along the conveyor.) As seen below, a similar phenomenon occurs for nutrient paths where the dilution near the end points is due to local and rapid recycling.

5.3. The Path Densities of PO_4 in the Base Equilibrium

[43] The second columns of Figures 9–11 show the PO_4 path densities for the data-assimilated ("base") equilibrium. While the absolute magnitudes of the path densities of water and PO_4 cannot meaningfully be compared (they have different dimensions as defined here), the patterns of the SANTZ→SANTZ path densities for PO_4 stand in sharp contrast to those for water. The signature of the particle export is strikingly evident in Figures 10 and 11, with a
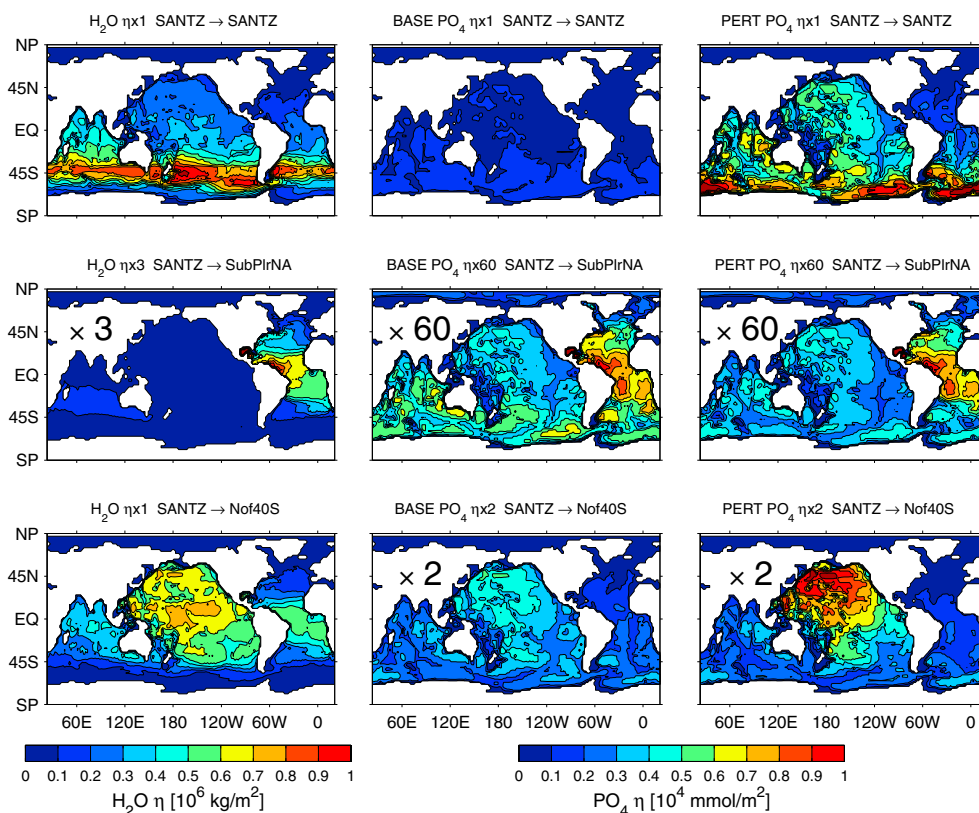
Figure 9. The vertically integrated water path density (left column) and export-to-uptake phosphate path density (column 2 for the base state, column 3 for the perturbed state) for SANTZ→SANTZ, SANTZ→SubPlrNA, and SANTZ→Nof40S transport, as indicated. The perturbation here consists of setting the uptake rate constant over the SANTZ region to a spatially uniform $\gamma = (10 \text{ days})^{-1}$. To use the same color scale for all panels, the path densities have been multiplied by the scale factor indicated in the titles and (if different from unity) on the plot panels.

SANTZ→SANTZ PO_4 path density that extends to the ocean bottom and well into the Northern Hemisphere in both the Atlantic and Pacific. The trough in the Atlantic zonally averaged SANTZ→SANTZ PO_4 path density between ∼2 and 4 km depth (Figure 10) is due to a corresponding trough in the PO_4 concentration (PHD, Figure 5) and reflects dilution of Southern-Ocean waters by comparatively nutrient-poor NADW.

[44] The Atlantic PO_4 paths (Figure 10) from the SANTZ to the North Atlantic are tightly confined to the thermocline north of 40°S with a pattern very similar to that of the corresponding water paths. This indicates that particle transport to the deep ocean plays little role in supplying the North Atlantic with nutrients from the Southern Ocean. In the Atlantic, SANTZ nutrients remineralized at depth are more likely to return to the Southern Ocean with the deep overturning circulation. This is consistent with our picture of Southern-Ocean nutrient trapping [PHD; *Oschlies et al.*, 2010] and also with the GCM results by *Sarmiento et al.* [2004] and *Marinov et al.* [2006] who suggested that it is transport within the thermocline that supplies Southern-Ocean nutrients to North-Atlantic production.

[45] Unlike in the Atlantic, the Pacific SANTZ→Nof40S and SANTZ→SubPlrNA PO_4 path densities (Figure 11) have patterns that are very different from their water counterparts.

The particle export manifests itself in a PO_4 path density that extends to the bottom throughout the Pacific. The SANTZ→SubPlrNA path density in the Pacific is roughly five times smaller than in the Atlantic and concentrated in the ACC, but spread throughout the deep Pacific with gradients such that the density increases with depth in the North Pacific and decreases with depth in the South Pacific. Compared to the water paths, the particle transport gives the SANTZ→Nof40S PO_4 paths greater access to the deep branch of the global interbasin circulation, which tends to spread the SANTZ PO_4 throughout the deep North Pacific. The maximum SANTZ→Nof40S PO_4 path densities lie at mid depths in the North Pacific, which is a holding pen of old water [*Holzer and Primeau*, 2006, 2008] in which the bulk of the world ocean's regenerated PO_4 tends to accumulate [PHD]. This mid-depth maximum of the PO_4 path density reflects the pattern of the total PO_4 concentration in the Pacific, which is preferentially weighted into the upper water column by the vertical profile of the particle-flux divergence.

5.4. The Path Densities of PO_4 in the Perturbed Equilibrium

[46] For the perturbed equilibrium with $\gamma = (10 \text{ days})^{-1}$ over the SANTZ (Figures 9–11, third columns), there is a dramatic increase of nearly an order of magnitude in the
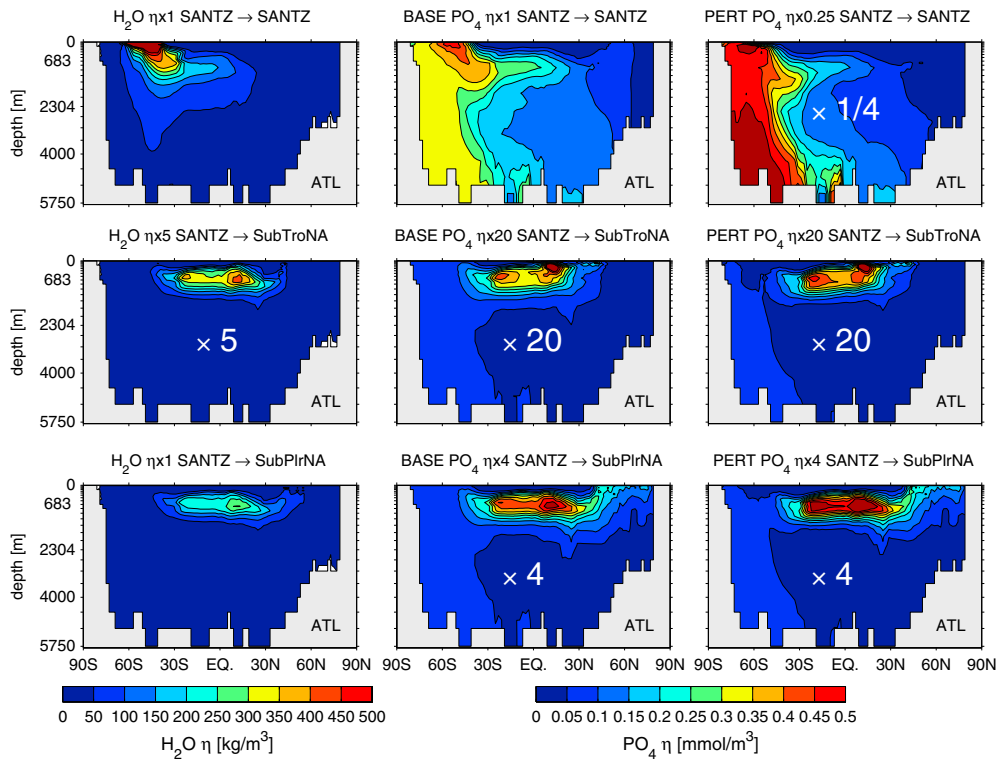
Figure 10. The Atlantic-sector zonally averaged water path density (left column) and phosphate path density (column 2 for base state, column 3 for the perturbed state) for SANTZ→SANTZ, SANTZ→SubTroNA, and SANTZ→SubPlrNA transport, as indicated. The perturbation here consists of setting the uptake rate over the SANTZ to a spatially uniform $\gamma = (10 \text{ days})^{-1}$. To use the same color scale for all panels, the path densities have been multiplied by the scale factor indicated in the titles and (if different from unity) on the plot panels.

SANTZ→SANTZ PO_4 path density in the Southern Ocean, particularly at depth: The increased SANTZ nutrient utilization greatly enhances the Southern-Ocean nutrient trapping. Because the particle export partly feeds into the abyssal AABW overturning cell, the deep trapped paths extend well into the Northern Hemisphere, particularly in the Pacific. (Note that the zonally averaged perturbed SANTZ→SANTZ path density has been scaled, for plotting purposes, by a factor of 1/4 relative to the unperturbed paths.)

[47] Interestingly, the perturbed SANTZ→SubPlrNA path density in the Pacific (Figure 11) is significantly reduced from its base state, particularly in the Southern Ocean where the ACC PO_4 paths have all but disappeared. By contrast, the perturbed Pacific SANTZ→Nof40S path density is increased by a factor of about 2 outside the Southern Ocean and decreased within the Southern Ocean. These changes in the Pacific suggest that the increased particle transport to depth shunts PO_4 from ACC paths to trapped SANTZ→SANTZ paths and to paths through the deep Pacific to eventual uptake north of 40°S. In the Atlantic (Figure 10), the perturbed SANTZ→SubTroNA and SANTZ→SubPlrNA PO_4 paths have nearly the same zonally averaged pattern as in the base state, but the amplitude of the pattern is somewhat increased (~10%), and the paths are vertically slightly more tightly confined, possibly reflecting the missing ACC PO_4 paths from the Pacific.

5.5. Factors Contributing to Changes in the PO_4 Path Density

[48] The increases of the SANTZ→Nof40S path density in the Pacific, and the SANTZ→SubTroNA and SubPlrNA path densities in the Atlantic, occur in spite of decreased thermocline PO_4 concentrations outside of the region of enhanced Southern-Ocean nutrient trapping. To establish what is driving these increases, Figure 12 shows the fractional changes in the path density $\bar{\eta}_I$ and its three factors, P_I, $f_I^{\downarrow}$, and $f_I^{\uparrow}$. (Note that outside of the SANTZ, the fractional change in P_I in the euphotic zone is also the fractional change in production, because $J = \gamma P_I$ and γ is unperturbed outside of the SANTZ.) Figure 12 shows that, in both basins, the increases in the path density are driven by a sharp increase in the fraction $f_I^{\downarrow}$ of nutrients last exported in the SANTZ, which dominates decreased PO_4 concentrations and decreased uptake fractions $f_I^{\uparrow}$.

[49] The changes shown in Figure 12 further quantify the enhanced Southern-Ocean nutrient trapping: Throughout the Pacific below ~2 km depth, the PO_4 concentration is increased by 10–30%, which indicates that in the Pacific the nutrient trapping extends throughout the basin via the deep overturning circulation. Because the trapping increases the fraction $f_I^{\uparrow}$ of PO_4 next utilized in the SANTZ, the fractions $f_I^{\uparrow}$ of next uptake in regions outside the Southern Ocean must decrease. The $\Delta f_I^{\uparrow}/f_I^{\uparrow}$ panels of Figure 12 show that this is indeed the case throughout most of the ocean.
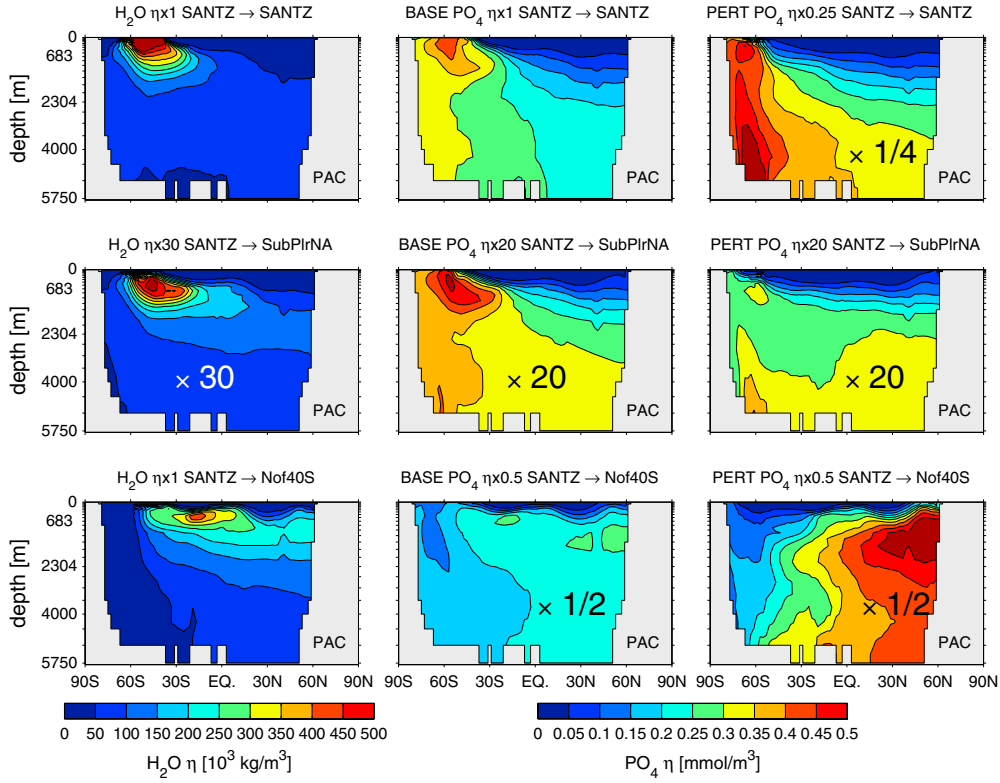
Figure 11. The Pacific-sector zonally averaged water path density (left column) and phosphate path density (column 2 for the base state, column 3 for the perturbed state) for SANTZ→SANTZ, SANTZ→SubPlrNA, and SANTZ→Nof40S transport, as indicated. The perturbation here consists of setting the uptake rate constant over the SANTZ to a spatially uniform $\gamma = (10\ \text{days})^{-1}$. To use the same color scale for all panels, the path densities have been multiplied by the scale factor indicated in the titles and (if different from unity) on the plot panels.

[50] The path density reveals the three-dimensional pathways of PO_4, while its volume integral quantifies the total amount of PO_4 in transit from last utilization in Ω_i to next uptake in Ω_f. In order to connect the changes in the path densities to the changes in the biological production rates, we require knowledge of the export-to-uptake timescales. To that end, we will now explore the timescales with which nutrients are transported, and how these change when the Southern-Ocean biology is perturbed.

6. Teleconnection Timescales

6.1. Flux Densities and Transit-time Distributions

[51] The timescales with which the productivity teleconnections between regions Ω_i and Ω_f are communicated are determined by the interplay between particle export in Ω_i, DOP to PO_4 conversion, transport, and biological uptake in Ω_f. We therefore distinguish three types of $\Omega_i \to \Omega_f$ pathways and associated transit times: (a) from last Ω_i surface contact as preformed PO_4 to first contact with the Ω_f surface layer (pre→srf), (b) from last production in Ω_i and subsequent regeneration to first contact with the Ω_f surface layer (exp→srf), and (c) from last production in Ω_i to next biological uptake in Ω_f (exp→upt). By "surface," we mean the two-layer euphotic zone here.

[52] Consider first the exp→upt case. The natural distribution function of the corresponding transit times is the uptake

flux in Ω_f of nutrients that were last utilized in Ω_i during the time interval $(\tau, \tau + d\tau)$ prior to uptake. This flux is simply the production rate in Ω_f sustained by nutrients last exported in Ω_i a time $\tau \in (\tau, \tau + d\tau)$ ago. We can think of the production rate as the one-way flux of PO_4 into the organisms that convert PO_4 to organic matter. When expressed per unit transit time τ, and spatially integrated over the destination region Ω_f, we denote the resulting one-way $\Omega_i \to \Omega_f$ flow-rate density per unit transit time by $\mathcal{J}(\tau, \Omega_i \to \Omega_f)$. In terms of the transit-time and surface-origin partitioned PO_4, $g_I^\downarrow(\mathbf{r}, \tau | \Omega_i) \equiv g_I^\downarrow(\mathbf{r}, t | \Omega_i, t - \tau)$ of equation (5), which is independent of t for steady flow, we thus have

$$\mathcal{J}(\tau, \Omega_i \to \Omega_f)d\tau = \int d^3r\ \Omega_f(\mathbf{r})\gamma(\mathbf{r})g_I^\downarrow(\mathbf{r}, \tau | \Omega_i). \quad (17)$$

[53] The one-way flux distribution for the exp→srf paths is computed in the same manner except that we use $g_{I,R}^\downarrow$, which differs from $g_I^\downarrow$ only by satisfying the boundary condition that $g_{I,R}^\downarrow = 0$ in the euphotic zone, which is enforced in practice by relaxing $g_{I,R}^\downarrow$ to zero in the euphotic layer with a timescale τ_a of a few seconds. Mathematically, γ is replaced at every point in the euphotic layer with $\gamma_a = 1/\tau_a$ in equations (1) and (17). The one-way flux distribution for the pre→srf paths is computed simply from the tracer response
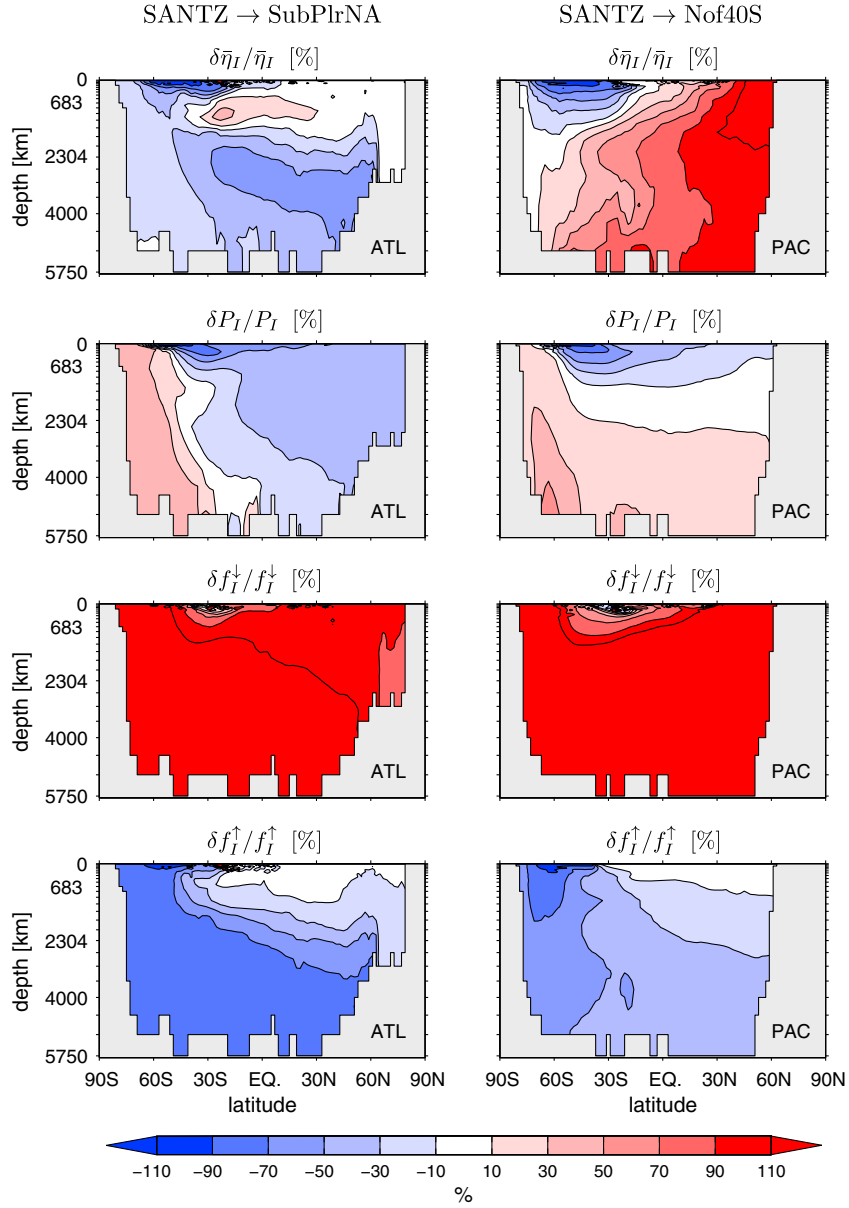
Figure 12. Fractional changes in the zonally averaged equilibrium phosphate path density, $\bar{\eta}_I = P_I f_I^{\downarrow} f_I^{\uparrow}$ and its three factors in response to increased SANTZ nutrient utilization. The changes plotted are for the productivity perturbation that sets the uptake rate constant over the SANTZ region to a spatially uniform $\gamma = (10 \text{ days})^{-1}$. The right column of plots is for the Atlantic-basin zonally averaged SANTZ→SubPlrNA paths, and the left column of plots is for the Pacific-basin zonally averaged SANTZ→Nof40S paths.

$g_{I,P}^{\downarrow}$ to the PO$_4$ concentration pulse $P_I(\mathbf{r})\Omega_i(\mathbf{r})\delta(\tau)$ subject to the boundary condition $g_{I,P}^{\downarrow} = 0$ in the euphotic layer, again enforced by setting $\gamma = \gamma_a$ in the euphotic layer. The one-way flux distribution for surface-to-surface (srf→srf) water paths is computed similarly, except that the response to $\Omega_i(\mathbf{r})\delta(\tau)$ is used. The pre→srf nutrient flux is thus very similar to the surface-to-surface water flux, except that in the pre→srf case the origin region is weighted with the preformed PO$_4$ distribution.

[54] The mean of the distribution $\mathcal{J}$, referred to here as the mean age on exit, directly connects the volume-integrated $\Omega_i \rightarrow \Omega_f$ path density to the corresponding $\Omega_i \rightarrow \Omega_f$ nutrient flow rate (equal to Ω_f production sustained by Ω_i nutrients in the case of the exp→upt paths) as we will now show.

6.2. Mean Nutrient Age on Exit and Mean Residence Time

[55] From the one-way flow-rate density distribution of interest, $\mathcal{J}(\tau, \Omega_i \rightarrow \Omega_f)$, the mean age on exit, Γ, is given by

$$\Gamma \equiv \frac{\langle \tau \mathcal{J} \rangle}{\langle \mathcal{J} \rangle}, \tag{18}$$

where $\langle . \rangle \equiv \int_0^{\infty} . d\tau$. "Exit" here simply means first contact with the Ω_f euphotic zone for the srf→srf (water), exp→srf, and pre→srf cases, and "exit" means biological uptake for the exp→upt case.

[56] From $\mathcal{J}$, we can immediately infer the mass of PO_4 in the ocean that is in transit from Ω_i to Ω_f with an interior residence time in the interval $(\tau, \tau + d\tau)$, which we denote by $\mathcal{R}(\tau, \Omega_i \rightarrow \Omega_f)d\tau$, so that $\mathcal{R}$ itself is a density with respect to τ. Because the $\Omega_i \rightarrow \Omega_f$ transit time τ is also the residence time of the mass $\mathcal{R}d\tau$ in the ocean interior, we know that this mass is flushed out of the interior in time τ with flow rate $\mathcal{J}d\tau$, so that

$$\mathcal{R}d\tau = \tau\mathcal{J}d\tau. \tag{19}$$

The transport mass $\mathcal{R}d\tau$ thus has a natural interpretation as a distribution of interior residence times [*Primeau and Holzer*, 2006] with a mean residence time, $\bar{\tau}$, given by

$$\bar{\tau} = \frac{\langle\tau\mathcal{R}\rangle}{\langle\mathcal{R}\rangle} = \frac{\langle\tau^2\mathcal{J}\rangle}{\langle\tau\mathcal{J}\rangle}. \tag{20}$$

The timescales Γ and $\bar{\tau}$ are easily computed for our steady-flow model via direct matrix inversion (see Appendix B) for the temporal moments of $g^{\downarrow}$ subject to appropriate boundary conditions, enforced here by modifying $\gamma(\mathbf{r})$.

6.3. Mean Age on Exit and Volume-integrated Path Density

[57] Note that the quantity $\langle\mathcal{J}\rangle$ is the $\Omega_i \rightarrow \Omega_f$ flow rate regardless of transit time, and $\langle\mathcal{R}\rangle = \langle\tau\mathcal{J}\rangle$ is the inventory of PO_4 that is in transit from $\Omega_i \rightarrow \Omega_f$ regardless of transit time (preformed PO_4 for pre$\rightarrow$srf, regenerated PO_4 for the exp$\rightarrow$srf, and total PO_4 for exp$\rightarrow$upt). Equation (18) is thus the familiar statement that the mean transport time is the mass/flux ratio

$$\Gamma = \frac{\langle\mathcal{R}\rangle}{\langle\mathcal{J}\rangle}. \tag{21}$$

[58] Equation (21) connects the mean age on exit with the path density $\bar{\eta}$ because the $\Omega_i \rightarrow \Omega_f$ inventory $\langle\mathcal{R}\rangle$ is also precisely the volume integral [*Holzer and Primeau*, 2008]

$$\langle\mathcal{R}\rangle = \int d^3r\, \bar{\eta}(\mathbf{r}, \Omega_i \rightarrow \Omega_f), \tag{22}$$

where $\bar{\eta}$ is the appropriate path density (e.g., for the srf$\rightarrow$srf water paths, $\bar{\eta} = \bar{\eta}_\rho$ given by equation (13)). Below, we will exploit this relationship to interpret changes in the mean

age on uptake for the exp$\rightarrow$upt paths, for which it is shown in Appendix D that the appropriate path density is $\bar{\eta} = \bar{\eta}_I + \bar{\eta}_O$, where $\bar{\eta}_I = P_I f_I^{\downarrow} f_I^{\uparrow}$ is the PO_4 path density of equation (15) and $\bar{\eta}_O \equiv P_O f_O^{\downarrow} f_O^{\uparrow}$ is the DOP path density, that is, the local concentration of DOP last produced in Ω_i that is next taken up (after remineralization) in Ω_f. However, to an excellent approximation, $\bar{\eta}_O$ can be neglected compared to $\bar{\eta}_I$ in the volume integral of equation (22) because much less phosphorus is present in organic form than in inorganic form. Specifically, $\bar{\eta}_O$ is only appreciable in, and close to, the euphotic zone of the origin region Ω_i, where its maximum local values are one to two orders of magnitude smaller than those of $\bar{\eta}_I$ (depending on the choices of Ω_i, Ω_f, and whether we perturb nutrient uptake). In all cases, the volume integral of $\bar{\eta}_O$ is about three orders of magnitude smaller that the volume integral of $\bar{\eta}_I$. Therefore, for the exp$\rightarrow$upt case, we can equate $\langle\mathcal{R}\rangle$ with the volume integral of the PO_4 path density $\bar{\eta}_I$ to an excellent approximation.

6.4. Timescales in the Base-state Equilibrium

[59] Table 1 collects the mean ages on exit, Γ, and mean residence times, $\bar{\tau}$, for the data-assimilated (unperturbed) equilibrium phosphorus cycle. We consider the (SANTZ, ANTZ)$\rightarrow$(SANTZ, ANTZ, SubTroNA, SubPlrNA, Nof40S) origin-to-destination pairs for the srf$\rightarrow$srf transport of water, and for the pre$\rightarrow$srf, exp$\rightarrow$srf, and exp$\rightarrow$upt transport of PO_4.

[60] Note that $\Gamma = 0$ for the water and preformed PO_4 paths when origin and destination regions coincide. This is because of the overwhelming contribution from eddy-diffusive paths with arbitrarily short residence times that connect any surface region with itself and that impart the corresponding flux-density distribution with a singularity at $\tau = 0$. If origin and receptor regions abut (e.g., SANTZ and Nof40S), the flux distribution has a weaker logarithmic singularity, which precludes a meaningfully computed mean age on exit. These singularities are not our focus here—for further details, see [*Hall and Holzer*, 2003; *Primeau and Holzer*, 2006; *Orbe et al.*, 2012]. Mean residence time is not affected by these singularities because it is mass (as opposed to flux) weighted, and the mean age on exit of regenerated PO_4 is also not subject to these flow singularities because of the finite timescale, κ^{-1}, for remineralization.

Table 1. The Mean Ages on Exit, Γ, and Mean Residence Times, $\bar{\tau}$, in Years for the (Unperturbed) Data-Assimilated Phosphorus Cycle[a]

Origin	Path Type		$\rightarrow$SANTZ Γ	$\bar{\tau}$	$\rightarrow$ANTZ Γ	$\bar{\tau}$	$\rightarrow$SubTroNA Γ	$\bar{\tau}$	$\rightarrow$SubPlrNA Γ	$\bar{\tau}$	$\rightarrow$Nof40S Γ	$\bar{\tau}$
SANTZ	H_2O	srf$\rightarrow$srf	0	906	138	1213	113	536	139	537	–	1127
SANTZ	PO_4	pre$\rightarrow$srf	0	930	118	1213	121	569	147	564	–	1173
SANTZ	PO_4	exp$\rightarrow$srf	47 ± 27	1248 ± 165	264 ± 61	1353 ± 71	163 ± 47	889 ± 264	192 ± 50	871 ± 253	283 ± 131	1518 ± 238
SANTZ	PO_4	exp$\rightarrow$upt	345 ± 78	2187 ± 53	646 ± 49	2235 ± 32	467 ± 80	2002 ± 104	523 ± 80	1972 ± 111	557 ± 118	2312 ± 80
ANTZ	H_2O	srf$\rightarrow$srf	86	1449	0	1355	502	1515	520	1489	1055	1945
ANTZ	PO_4	pre$\rightarrow$srf	93	1452	0	1357	516	1526	534	1500	1070	1950
ANTZ	PO_4	exp$\rightarrow$srf	102 ± 42	1377 ± 52	76 ± 34	1331 ± 31	339 ± 74	1322 ± 123	360 ± 73	1285 ± 128	845 ± 129	1853 ± 58
ANTZ	PO_4	exp$\rightarrow$upt	506 ± 51	2237 ± 19	444 ± 51	2244 ± 13	660 ± 53	2152 ± 40	703 ± 53	2133 ± 44	926 ± 64	2443 ± 26

[a]Rows identify the origin region and path type, while the main columns identify the receptor region. The timescales are tabulated for four types of transport: the transport of water (H_2O) from the origin surface to the receptor surface (srf$\rightarrow$srf), the transport of preformed PO_4 from the origin surface to first contact with the receptor euphotic layer (pre$\rightarrow$srf), the transport of PO_4 from last utilization in the origin region to first contact with the receptor surface layer (exp$\rightarrow$srf), and the transport of phosphate from last utilization to next uptake (exp$\rightarrow$upt). The uncertainties quoted are due to the uncertainties in the phosphorus cycling parameters and estimated as described in Appendix B.

6.4.1. Mean Ages on Exit, Γ

[61] The SANTZ→SANTZ and ANTZ→ANTZ exp→srf mean ages on exit are 47 and 76 years, while the corresponding exp→upt mean ages on exit are an order of magnitude longer (345 and 444 years). The ANTZ→ANTZ mean ages are modestly longer than the SANTZ→SANTZ ages because ANTZ particle transport does not inject the DOP into upwelling circumpolar deep water as efficiently as SANTZ particle transport. The mean ages on uptake are much longer than the mean ages on exit into the euphotic zone because of the extra time required for PO_4 to "find" the uptaking plankton.

[62] For transport from the SANTZ to the North Atlantic, the water and preformed mean ages on exit are roughly 100 years, with older ages for transport to the more distant SubPlrNA than to the SubTroNA. The corresponding exp→srf mean ages on exit are about 1.3 times longer for transport to the North Atlantic and 2 times longer for transport to Nof40S, which is primarily transport within the Pacific. The fact that the exp→srf ages are longer than the srf→srf and pre→srf ages is due to SANTZ particle transport injecting DOP into the slower deeper circulation, while water and preformed PO_4 are transported out of the SANTZ primarily via more rapidly circulating mode waters. The exp→upt mean ages are yet longer by a factor or roughly 2–3, as expected because of the extra time to find the uptaking organisms.

[63] The srf→srf and pre→srf timescales for paths beginning in the ANTZ are very different from those beginning in the SANTZ because the ANTZ ventilates AABW and the deep overturning circulation, while the SANTZ ventilates the faster mode waters. Thus, water and preformed mean ages on exit for ANTZ → North Atlantic are roughly 500 years (four times longer than for the SANTZ case), and roughly 1000 years for ANTZ→Nof40S.

[64] The effect of the particle transport on the mean transit times to remote receptor locations is also strikingly different for ANTZ and SANTZ origin. For transport from the ANTZ, the exp→srf mean age on exit is in fact shorter than the pre→srf mean age on exit by a factor of roughly 1.5 for exit in the North Atlantic and by a factor of ~1.3 for exit Nof40S. This phenomenon has a simple explanation: Some of the preformed PO_4 is carried with the AABW forming near Antarctica into the slow, deep overturning circulation. By contrast, there is relatively little production at the deep-water formation sites near Antarctica (at least in our model) so that very little DOP, and hence very little regenerated PO_4, is directly injected into AABW. Most of the ANTZ production occurs at its northern edge in regions of mean upwelling, and much of the resulting regenerated PO_4 accesses the shallower thermocline paths much like water and nutrients from the SANTZ (this picture has been confirmed by looking at the corresponding path densities, not shown). The fact that the regenerated nutrients from the northern edge of the ANTZ are not simply carried south with the bulk-advective overturning underscores the importance of quasi-horizontal eddy diffusion through which ANTZ waters and nutrients have access to the SANTZ where they feed into mode waters. As expected, the exp→upt mean ages are yet longer by a factor of ~1.7 for transport to the North Atlantic, and by a factor of ~1.1 for transport to Nof40S.

6.4.2. Mean Residence Times, $\bar{\tau}$

[65] The overall pattern discussed for the mean age on exit, Γ, also applies to the mean residence times, $\bar{\tau}$, except that $\bar{\tau}$ is much longer than Γ. For paths to remote receptors starting in the SANTZ, $\bar{\tau}$ is four to five times longer than the corresponding Γ, and for the paths starting in the ANTZ, $\bar{\tau}$ is two to four times longer than the corresponding Γ.

[66] The differences between $\bar{\tau}$ and Γ are a direct consequence of the multiplicity of advective–diffusive paths in the ocean, which imparts the flux-density distribution $\mathcal{J}$ with a finite width. To illustrate the character of the flux-density distribution, Appendix E shows $\mathcal{J}$ for SANTZ → (Sub-PlrNA, SubTroNA) transport and the three nutrient path types considered (pre→srf, exp→srf, exp→upt). The distributions are broad and skewed with exponential tails whose decay time depends on the path type. The connection between Γ and $\bar{\tau}$ is explored in detail by *Holzer et al.* [2012]. In a nutshell, $\bar{\tau}$ is the mean $\Omega_i \to \Omega_f$ transit time averaged over the population of PO_4 (or water) molecules residing in the interior, while Γ averages over the population that is exiting the interior at Ω_f. Because a greater amount of PO_4 (or water) is carried by the longer paths (proportional to $\mathcal{R} = \tau \mathcal{J}$), averaging over the interior population with distribution $\mathcal{R}$ gives longer mean times than averaging over the exiting population with distribution $\mathcal{J}$.

6.5. Equilibrium Timescales with Perturbed Southern-Ocean Utilization

[67] To connect the changes in the path density seen in section 5 with the changes in productivity teleconnections when SANTZ nutrient utilization is perturbed, we now examine the effect of such perturbations on the transport timescales. Because of its simple connection to the volume-integrated path density, $\langle \mathcal{R} \rangle$, and the corresponding nutrient flow rate, $\langle \mathcal{J} \rangle$, we focus on the export→uptake mean age on exit, Γ. From equation (18) it follows that changes $\delta\Gamma$, $\delta\langle\mathcal{R}\rangle$, and $\delta\langle\mathcal{J}\rangle$ induced by perturbing the phosphorus cycle obey, to first order,

$$\frac{\delta\Gamma}{\Gamma} \simeq \frac{\delta\langle\mathcal{R}\rangle}{\langle\mathcal{R}\rangle} - \frac{\delta\langle\mathcal{J}\rangle}{\langle\mathcal{J}\rangle}. \tag{23}$$

Thus, increases in Γ result from an increased mass $\langle\mathcal{R}\rangle$ of $\Omega_i \to \Omega_f$ PO_4 and/or a decreased $\Omega_i \to \Omega_f$ flow rate $\langle\mathcal{J}\rangle$.

[68] Table 2 tabulates the three terms of equation (23) for the SANTZ→(SANTZ, SubTroNA, SubPlrNA, Nof40S) export-to-uptake paths and three types of perturbations: $\gamma(\mathbf{r})$ has been perturbed over the SANTZ by either setting $\gamma(\mathbf{r})$ to $(10 \text{ days})^{-1}$ as in section 5, or by multiplying $\gamma(\mathbf{r})$ by 10 or by 0.1. The $\gamma(\text{SANTZ}) = (10 \text{ days})^{-1}$ and the $\gamma(\text{SANTZ}) \to 10 \times \gamma(\text{SANTZ})$ perturbations are qualitatively similar, both representing enhanced nutrient utilization. For enhanced SANTZ utilization, the mean age on uptake for the SANTZ→SANTZ trapped paths becomes roughly 50–60% shorter, which happens in spite of a two-to threefold (248% and 344%) increase in the trapped mass $\langle\mathcal{R}\rangle$ because of the strongly enhanced SANTZ→SANTZ flow rate $\langle\mathcal{J}\rangle$. When utilization is reduced by a factor of 10, the mean age on uptake for the SANTZ→SANTZ trapped paths increases by roughly 50%, with the effects of a reduced SANTZ→SANTZ PO_4 mass $\langle\mathcal{R}\rangle$ and decreased SANTZ→SANTZ flow rate $\langle\mathcal{J}\rangle$ again opposing each other

Table 2. The Mean Age on Uptake $\Gamma = \langle \mathcal{R} \rangle / \langle \mathcal{J} \rangle$ in the Unperturbed (Base) Data-Assimilated Equilibrium for the Export-to-Uptake Pathways Indicated, and the Percentage Changes in Γ and the First-Order Terms Contributing to This Change When SANTZ Nutrient Utilization Is Perturbed[a]

Path	base Γ[yrs]	$\gamma(\text{SANTZ})=(10\text{ days})^{-1}$			$\gamma(\text{SANTZ}) \times 10$			$\gamma(\text{SANTZ}) \times 0.1$		
		$\frac{\delta\Gamma}{\Gamma}$	$\frac{\delta\langle\mathcal{R}\rangle}{\langle\mathcal{R}\rangle}$	$-\frac{\delta\langle\mathcal{J}\rangle}{\langle\mathcal{J}\rangle}$	$\frac{\delta\Gamma}{\Gamma}$	$\frac{\delta\langle\mathcal{R}\rangle}{\langle\mathcal{R}\rangle}$	$-\frac{\delta\langle\mathcal{J}\rangle}{\langle\mathcal{J}\rangle}$	$\frac{\delta\Gamma}{\Gamma}$	$\frac{\delta\langle\mathcal{R}\rangle}{\langle\mathcal{R}\rangle}$	$-\frac{\delta\langle\mathcal{J}\rangle}{\langle\mathcal{J}\rangle}$
SANTZ→SANTZ	345	−64%	+344%	−1141%	−51%	+248%	−609%	+47%	−97%	+98%
SANTZ→SubTroNA	467	−23%	−23%	0%	−30%	−9%	−30%	+36%	−73%	+80%
SANTZ→SubPlrNA	523	−22%	−14%	−10%	−27%	0%	−37%	+32%	−74%	+80%
SANTZ→Nof40S	557	+45%	+32%	+9%	+12%	25%	−12%	+20%	−74%	+78%

[a]Three perturbations of the SANTZ uptake rate constants are considered, as indicated.

and with the changes in $\langle \mathcal{J} \rangle$ again dominating. Note that the percentages do not simply add because the first-order equation (23) is only accurate for small perturbations.

[69] For paths to the North Atlantic (SubTroNA and SubPlrNA) the mean age on uptake decreases by roughly 20–30% with increased SANTZ utilization, and increases by roughly 30% with decreased SANTZ utilization. Consistent with our findings for the path density, the $\gamma = (10 \text{ days})^{-1}$ perturbation reduces the total number of paths to the North Atlantic by shunting paths into trapped SANTZ→SANTZ routes or into SANTZ→Nof40S routes in the Pacific. At the same time, the increased SANTZ export rate increases the corresponding flow rate (the production sustained by SANTZ nutrients), both of which act to shorten the mean age on exit. Thus, increasing Southern-Ocean nutrient utilization speeds up the teleconnections with the North Atlantic. When SANTZ production is reduced by a factor of 10, the number of paths to the North Atlantic drop by about 70%, but are compensated by even greater decreases in the SANTZ-sustained production, resulting in mean ages at uptake that are roughly 30% longer. Thus, weakening Southern-Ocean production slows the teleconnections to the North Atlantic.

[70] The SANTZ→Nof40S export-to-uptake transport takes place primarily in the Pacific, where the dominant effect of an increased SANTZ utilization is an increase in the number of SANTZ→Nof40S paths as noted in section 5, resulting in increased mean age at uptake. Decreased SANTZ utilization also increases the mean age at uptake, with decreased SANTZ-sustained production north of 40°S dominating a decreased number of paths. Thus, both increased and decreased Southern-Ocean nutrient utilization slows the teleconnections with the Pacific north of 40°S, with the competition between the $\Omega_i \rightarrow \Omega_f$ PO$_4$ mass $\langle \mathcal{R} \rangle$ and flow rate $\langle \mathcal{J} \rangle$ being won by $\delta\langle\mathcal{R}\rangle/\langle\mathcal{R}\rangle$ for increased SANTZ utilization, and by $-\delta\langle\mathcal{J}\rangle/\langle\mathcal{J}\rangle$ for decreased SANTZ utilization. Interestingly, the SANTZ→Nof40S mean age at uptake appears to be near a local minimum in the unperturbed state with respect to perturbations in the SANTZ uptake rate constant.

7. Summary and Conclusions

[71] We quantified the ocean's productivity teleconnections with the Southern Ocean and the nutrient transport pathways and timescales that mediate these teleconnections. This was accomplished using a global data-assimilated model with jointly optimized circulation and phosphorus cycling as described separately by *Primeau et al.* [2012]. Because the

model is optimized to fit the observed concentration fields for CFC-11, T, S, PO$_4$, and natural radiocarbon very closely, we expect that its transport is subject to fewer biases than the transport of free-running ocean models, which is sensitive to subgrid parameterizations and wind stress [*Gnanadesikan et al.*, 2002, 2004; *Marinov et al.*, 2008; *Palter et al.*, 2010].

[72] The linearity of the phosphorus cycling model permitted a novel application of Green-function techniques to partition PO$_4$ according to the locations and times since last biological uptake, and the locations and times to next biological uptake, in addition to the locations and times of last and to next contact with the euphotic zone. From the partitioned PO$_4$, a set of new diagnostics was constructed to quantify the phosphorus cycling in the data-assimilated equilibrium and to investigate idealized perturbed equilibrium states with enhanced Southern-Ocean nutrient utilization.

[73] Teleconnections were quantified in terms of the local fraction of the production that is sustained by nutrients last utilized in each region of a global tiling of the euphotic zone. In the extratropical Northern Hemisphere, the subpolar North Atlantic has the strongest teleconnection with the Southern Ocean, with Southern-Ocean export sustaining $29 \pm 6\%$ of North-Atlantic new production. The subtropical gyres of the Atlantic and Pacific have the weakest teleconnections with the Southern Ocean, as expected for regions of mean downwelling. In spite of being oligotrophic, the large area of the subtropical Atlantic still supports significant new production, in total about half as much as the Atlantic subpolar gyre, and nutrients last exported in the Southern Ocean sustain $14 \pm 6\%$ of that new production.

[74] Forcing nearly complete nutrient utilization in the SANTZ by setting its production rate constant to a spatially uniform $(10 \text{ days})^{-1}$ leads to nutrient trapping in the Southern Ocean and a corresponding production decline in the rest of the world oceans [see also *Primeau et al.*, 2012]. In the North Atlantic, production drops by 40–50%, but the fraction supported by nutrients last exported in the Southern Ocean nearly doubles.

[75] Nutrient pathways from region Ω_i to region Ω_f were quantified by the path density of PO$_4$, which is the local concentration of PO$_4$ that was last utilized in Ω_i and that will next be taken up in Ω_f. The teleconnections with the North Atlantic are primarily mediated by thermocline paths in the Atlantic and by paths within the ACC in the Pacific. By contrast, the teleconnections with anywhere north of 40°S are primarily associated with paths below the thermocline in the North Pacific. The ratio of the $\Omega_i \rightarrow \Omega_f$ PO$_4$ mass, $\langle \mathcal{R} \rangle$, and the $\Omega_i \rightarrow \Omega_f$ export-to-uptake nutrient flow rate, $\langle \mathcal{J} \rangle$, is the mean PO$_4$ age on uptake, Γ. Changes in Γ due to

perturbations in the nutrient cycle could thus be understood in terms of the competition between changes in $\langle \mathcal{R} \rangle$ and $\langle \mathcal{J} \rangle$.

[76] Enhanced nutrient trapping, in response to forcing nearly complete SANTZ utilization, short circuits the ACC paths to the North Atlantic, decreasing the total amount of SANTZ-exported PO_4 destined for uptake in the North Atlantic. This, in concert with an increased export-to-uptake flow rate to the North Atlantic, reduces the mean age of the nutrients on uptake by 20–30%, that is, the nutrient trapping speeds up the Southern Ocean's teleconnections with the North Atlantic. For the Pacific paths, the nutrient trapping has the opposite effect, with greatly enhanced SANTZ particle export feeding into the deep Pacific overturning cell, which increases by $\sim$30% the number of paths to uptake north of 40°S. The increased path density dominates the corresponding changes in flow rate, increasing the mean age on uptake or, equivalently, slowing the Southern Ocean's teleconnections with the ocean north of 40°S.

[77] To quantify the interaction of biological production with the circulation through spatially inhomogeneous particle export and PO_4 uptake, we also computed the mean age of preformed and regenerated nutrients on exit back into the euphotic surface layer (preformed-to-surface and export-to-surface). The mean ages on exit into the surface layer are younger than the mean ages on uptake, with the longer mean time to uptake quantifying the availability of plankton for intercepting the PO_4 paths. For export from the SANTZ, export-to-surface mean ages are longer than preformed-to-surface mean ages because the particle export provides access to the slower deep circulation. However, for export from the ANTZ, export-to-uptake ages are shorter than preformed-to-surface ages. This is because most of the ANTZ production occurs near the northern edge of the ANTZ so that ANTZ-utilized nutrients have access, in part through eddy diffusion, to the relatively fast flowing mode waters ventilated in the SANTZ, while most ANTZ preformed PO_4 is transported northward by the relatively slower abyssal circulation after having been carried to depth in deepwater formation sites near Antarctica.

[78] While for advectively dominated flow along a single pathway, one expects the mean age on exit Γ and the mean interior residence time $\bar{\tau}$ to be similar, we find that $\Gamma \ll \bar{\tau}$ by a factor ranging from $\sim$2 to $\sim$5 for the remote connections with the SANTZ. This underscores the importance of mixing through particle export and eddy diffusion, which results in broad, skewed nutrient transit-time distributions with long tails. A consequence of this skewness is that the most probable transit times from SANTZ export to North-Atlantic uptake are an order of magnitude shorter than the corresponding mean transit times ("export-to-uptake mean ages on exit") of 470 ± 80 and 520 ± 80 years to uptake in the subtropical and subpolar gyres, respectively.

[79] It is important to contrast our work with previous studies on the high-latitude controls of the ocean's global nutrient cycles. While we were in part motivated by the large sensitivity of North-Atlantic production to Southern-Ocean nutrient utilization seen by *Sarmiento et al.* [2004], the key questions addressed in that study and its recent expansion by *Palter et al.* [2010] were related to how nutrients continually exported to depth are returned to the pycnocline to close the global nutrient cycle. In particular, these authors highlighted the importance of SAMW as a source of

nutrients to the upper ocean, and *Palter et al.* [2010] used a suite of free-running models with different parameterizations and wind stresses to bracket the amount of low-latitude production fueled by SAMW nutrients. By contrast, here we focused on how biological production in the Southern Ocean is connected to the biological production in other regions. We therefore label nutrients primarily according to where they were last utilized, while *Palter et al.* [2010] label nutrients for particular water masses, such as southern-hemisphere, high-latitude SAMW.

[80] Our study and the study by *Palter et al.* [2010] thus emphasize complementary, but fundamentally different aspects of the nutrient cycle, and results from the two studies cannot directly be compared. For example, for the model *Palter et al.* [2010] judge to have the most realistic tracer distributions, SAMW nutrients sustain 75% of the low-latitude production with a timescale of 40 years, while we estimate that SANTZ-utilized nutrients sustain $\sim$12.5=$\frac{1}{6}$ 75% of the low-latitude model production with a timescale of $\sim$500 years. These differences can straightforwardly be understood as stemming from the fact that very different nutrient populations are being considered. Assuming that the production in the two cases is similar, we estimate, from the product of timescale and low-latitude production supported, that the steady-state pool of SANTZ-utilized PO_4 is larger than the pool of SAMW-tagged nutrients by a factor of $\sim$2. This is because SAMW-tagged nutrients lose their SAMW label when they are transported below the lower SAMW density bound south of $\sim$30°S, while the particle transport and subsequent remineralization injects a significant fraction of SANTZ-utilized nutrients deep into the water column building up a larger mass $\langle \mathcal{R} \rangle$ of nutrients eventually taken up at low latitudes. More importantly, because a significant fraction of the SANTZ-utilized nutrients are sent into the slow, deep flow, their mean transit time to low-latitude uptake (mean age at uptake, $\langle \mathcal{R} \rangle / \langle \mathcal{J} \rangle$) is $\sim$12 times longer than the corresponding mass-to-flux ratio of 40 years for the SAMW-tagged nutrients. Therefore, the low-latitude production supported by the SANTZ-utilized nutrients, $\langle \mathcal{J} \rangle = \langle \mathcal{R} \rangle / \Gamma$, is only $\sim$2/12 of the production sustained by SAMW-tagged nutrients.

[81] The use of a data-assimilated model, with a jointly optimized circulation and phosphorus cycle, gives us confidence that our results apply to the real ocean, but it is important to keep in mind the limitations of our study. The phosphorus cycle and circulation were modeled as being steady and, therefore, miss important effects of seasonality. In particular, our annually averaged model does not capture the phasing of seasonal productivity bursts with seasonal mode-water formation, which has been shown to be important for the transport of organic matter and nutrients in the subtropical gyres [e.g., *Palter et al.*, 2005; *Krémeur et al.*, 2009]. Our model also approximates the phosphorus cycling parameters (σ, κ, b) as globally uniform, which we acknowledge is only a rough approximation for the sake of simplicity. A particularly subtle assumption is that it suffices to characterize remineralization by a single timescale κ^{-1} on the order of six months. While this insures that the optimized production rates include little rapid recycling of DOP in the euphotic zone, a process that is unconstrained by the large-scale PO_4 fields assimilated, differences between model uptake and new production nevertheless depend on the actual value

of κ. A more comprehensive data assimilation could allow the parameters to vary spatially [e.g., *Schlitzer*, 2002], and measurements of dissolved organic matter could be used to constrain remineralization rates [e.g., *Williams et al.*, 2011; *Hansell et al.*, 2012].

[82] Separate assumptions enter our perturbation experiments, which were not only highly idealized in their spatial structure, but also in their neglect of feedbacks on biology outside the perturbation region. The tacit assumption is that PO_4 is always a limiting nutrient so that the ratio of production to PO_4 cannot change, which may not be the case in regions where other nutrients become limiting. In future studies, we will aim to systematically relax the assumptions and approximations made here and also to extend our analysis to the silicon and nitrogen cycles in order to shed light on how nutrient transport controls elemental ratios in the ocean. We believe that our approach of simple linear nutrient cycling models, and their Green-function based analysis in terms of partitioned nutrients, nutrient path densities, and transport timescales, will remain very useful for quantifying and understanding the ocean's biogeochemical cycles.

Appendix A: Table of Key Symbols and Definitions

Symbol	SI unit	Definition
DOP	–	acronym for Dissolved Organic Phosphorus
P_I	mol m^{-3}	concentration of phosphorus in inorganic form (PO_4)
P_O	mol m^{-3}	concentration of phosphorus in dissolved organic form (DOP)
P	mol m^{-3}	concentration vector for the combined (PO_4, DOP) system
J	mol s^{-1} m^{-3}	phosphate uptake rate per unit volume
γ	s^{-1}	phosphate uptake rate constant; $\gamma \equiv J/P_I$
κ	s^{-1}	DOP remineralization rate constant; $\kappa = (0.5 \text{ years})^{-1}$
σ	dimensionless	fraction of the biological uptake allocated as a DOP source to the euphotic zone; $\sigma = 1/3$
b	dimensionless	exponent of the power-law particle-flux profile; $b = 0.70$
$\mathcal{T}$	s^{-1}	advection–diffusion transport operator (gives divergence of advective–diffusive flux when acting on a concentration field) —see equation (1)
A	s^{-1}	combined advection–diffusion, organic particle transport, and DOP to PO_4 conversion operator— see equation (2)
$\mathcal{S}$	s^{-1}	source operator that acts on the PO_4 field to convert production into the vertically distributed DOP concentration source— see equation (1)
S	mol s^{-1} m^{-3}	DOP source field, $S \equiv \mathcal{S}P_I$
S	mol s^{-1} m^{-3}	source vector for the combined (PO_4, DOP) field—see equation (2); $\mathbf{S} \equiv [0, S]^T$

(Continues)

(Continued)

$\mathbf{G}(\mathbf{r}, t \vert \mathbf{r}', t')$	m^{-3}	Green function of the two-tracer system (1) that propagates a unit source, at source point $\mathbf{r}'$ and source time t', to the concentration response at field point $\mathbf{r}$ and field time t—see equations (3) and (4) and Appendix B
Ω_i	dimensionless	mask and label for a specified origin region of the euphotic zone (subscript i for 'initial')
Ω_f	dimensionless	mask and label for a specified destination region of the euphotic zone (subscript f for 'final')
t_i	s	time when at Ω_i; infinitesimal increment dt_i
t_f	s	time when at Ω_f; infinitesimal increment dt_f
$\Omega_i \rightarrow \Omega_f$	–	shorthand for "from region Ω_i to region Ω_f"
$g_X^{\downarrow}(\mathbf{r}, t \vert \Omega_i, t_i)dt_i$	mol m^{-3}	concentration of portion of PO_4 (subscript $X = I$) or DOP (subscript $X = O$) at ($\mathbf{r}$,t) due to production in Ω_i during time interval $(t_i, t_i + dt_i)$—see equation (5)
$\mathcal{G}_X(\mathbf{r}, t \vert \Omega_i, t_i)dt_i$	dimensionless	fraction of PO_4 (subscript $X = I$) or DOP (subscript $X = O$) at ($\mathbf{r}$,t) last taken up in region Ω_i during time interval $(t_i, t_i + dt_i)$— see equation (6)
$g_X^{\uparrow}(\mathbf{r}, t \vert \Omega_f, t_f)dt_f$	mol m^{-3}	concentration of portion of PO_4 (subscript $X = I$) or DOP (subscript $X = O$) at ($\mathbf{r}$,t) that will next be taken up in Ω_f during time interval $(t_f, t_f + dt_f)$—see equation (7)
$\widetilde{G}_X(\mathbf{r}, t \vert \Omega_f, t_f)dt_f$	dimensionless	fraction of PO_4 (subscript $X = I$) or DOP (subscript $X = O$) at ($\mathbf{r}$,t) that will next be taken up in Ω_f during time interval $(t_f, t_f + dt_f)$— see equations (8) and (9)
$f_X^{\downarrow}(\mathbf{r}, t \vert \Omega_i)$	dimensionless	fraction of PO_4 (subscript $X = I$) or DOP (subscript $X = O$) at ($\mathbf{r}$,t) last taken up in region Ω_i regardless of when the uptake occurred—see equation (11)
$f_X^{\uparrow}(\mathbf{r}, t \vert \Omega_f)$	dimensionless	fraction of PO_4 (subscript $X = I$) or DOP (subscript $X = O$) at ($\mathbf{r}$,t) that will next be taken up in region Ω_f regardless of when the uptake will occur—see equation (12)
$\bar{\eta}_\rho(\mathbf{r}, \Omega_i \rightarrow \Omega_f)$	kg m^{-3}	water path density at $\mathbf{r}$ or, equivalently, the density of the water at $\mathbf{r}$ that is in transit from Ω_i to Ω_f, regardless of transit time—see equation (13)
$\bar{\eta}_I(\mathbf{r}, \Omega_i \rightarrow \Omega_f)$	mol m^{-3}	phosphate path density at $\mathbf{r}$ or, equivalently, the concentration of PO_4 at $\mathbf{r}$ that is in transit from Ω_i to Ω_f, regardless of transit time—see equation (15)
$\bar{\eta}_O(\mathbf{r}, \Omega_i \rightarrow \Omega_f)$	mol m^{-3}	DOP path density at $\mathbf{r}$ or, equivalently, the concentration of DOP at $\mathbf{r}$ that is in transit from Ω_i to Ω_f, regardless of transit time—see Appendix E
$g_I^{\downarrow}(\mathbf{r}, \tau \vert \Omega_i)$	mol m^{-3} s^{-1}	simplified notation for $g_I^{\downarrow}(\mathbf{r}, t \vert \Omega_i, t - \tau)$ used for steady flow for which there is no dependence on the time t

(Continues)

(Continued)

$\mathcal{J}(\tau, \Omega_i \to \Omega_f)$	mol s^{-2} or kg s^{-2}	flow rate from Ω_i to Ω_f in transit-time interval $(\tau, \tau + d\tau)$ per unit transit time, τ—see equation (17); the flow rate is $\mathcal{J}d\tau$
$\mathcal{R}(\tau, \Omega_i \to \Omega_f)$	mol s^{-1} or kg s^{-1}	amount (measured as moles or mass) of nutrients or water that is in transit from Ω_i to Ω_f in transit-time interval $(\tau, \tau + d\tau)$ per unit transit time, τ—see equation (19); the amount, also referred to as transport mass, is $\mathcal{R}d\tau$
τ	s	transit time from the euphotic zone through the interior back to the euphotic zone and hence residence time below the euphotic zone; $\tau \equiv t_f - t_i$
$\langle . \rangle$	s	notation for the integral operator for integrating over all transit times of the quantity in brackets, that is, $\langle . \rangle \equiv \int_0^\infty . d\tau$.
Γ	s	mean age on exit after transport from Ω_i to Ω_f or, equivalently, the $\Omega_i \to \Omega_f$ flow-rate-weighted mean transit time—see equation (18)
$\bar{\tau}$	s	mean residence time in the ocean interior (below the euphotic zone) while in transit from Ω_i to Ω_f or, equivalently, the $\Omega_i \to \Omega_f$ transport-mass-weighted mean transit time—see equation (20)
ξ	s	point-to-point transit time; $\xi \equiv t - t'$—see Appendix B
Nof40S	–	global ocean north of latitude 40°S
ANTZ	–	antarctic zone—see Figure 2
SANTZ	–	subantarctic zone—see Figure 2
SubPlrNA	–	subpolar North-Atlantic region—see Figure 5
SubTroNA	–	subtropical North-Atlantic region—see Figure 5

Appendix B: Key Mathematical Details for Partitioning PO₄ and DOP

[83] Here we provide the key equations used for computing the transit-time and surface-origin partitioned phosphate and DOP fields. The analysis can be divided into two separate problems (see Figure 1): (a) The "in problem" that tracks nutrients and DOP at $(\mathbf{r}, t)$ backward in time to where they were last utilized (or at the surface as preformed nutrients), and (b) the "out problem" that tracks nutrients and DOP at $(\mathbf{r}, t)$ forward in time to where they will be utilized next (or make subsequent contact with the euphotic zone). For numerically efficient computation, the in problem is formulated as a forward integration, and the out problem as an integration in the time-reverse adjoint flow, as we now describe in detail.

The "In" Problem

[84] Equation (4) for the fundamental Green function can be recast as an initial-value problem by integrating in time

to $t' + \varepsilon$ in the limit as ε goes to zero. Specializing to steady flow, we have $\mathbf{G}(\mathbf{r}, t | \mathbf{r}', t') \to \mathbf{G}(\mathbf{r}, \xi | \mathbf{r}')$ because for steady flow the Green function can depend on t and t' only on $\xi = t - t'$. The steady initial value problem then becomes

$$(\partial_\xi + \mathbf{A})\mathbf{G}(\mathbf{r}, \xi | \mathbf{r}') = 0, \qquad (24)$$

with initial condition

$$\mathbf{G}(\mathbf{r}, 0 | \mathbf{r}') = \mathbf{I}\delta(\mathbf{r} - \mathbf{r}'). \qquad (25)$$

The partitioned PO₄/DOP last utilized in region Ω_i per unit transit time, denoted by $\mathbf{g}^\downarrow = \left[g_I^\downarrow, g_O^\downarrow\right]^T$, are related to $\mathbf{G}$ through equation (5), which for steady flow becomes

$$\mathbf{g}^\downarrow(\mathbf{r}, \xi | \Omega_i) = \int d^3 r' \mathbf{G}(\mathbf{r}, \xi | \mathbf{r}') \begin{bmatrix} 0 \\ S(\mathbf{r}')\Omega_i(\mathbf{r}') \end{bmatrix}. \qquad (26)$$

The corresponding initial value problem for $\mathbf{g}^\downarrow$ is therefore

$$(\partial_\xi + \mathbf{A})\mathbf{g}^\downarrow(\mathbf{r}, \xi | \Omega_i) = 0, \qquad (27)$$

with the initial condition

$$\mathbf{g}^\downarrow(\mathbf{r}, 0 | \Omega_i) = \begin{bmatrix} 0 \\ S(\mathbf{r})\Omega_i(\mathbf{r}) \end{bmatrix}. \qquad (28)$$

Temporal moments $\left\langle \xi^n \mathbf{g}^\downarrow \right\rangle \equiv \int_0^\infty \xi^n \mathbf{g}^\downarrow d\xi$ can easily be computed by multiplying the equation of motion (27) for $\mathbf{g}^\downarrow$ by ξ^n and integrating over ξ. One obtains the set of equations

$$\mathbf{A}\left\langle \mathbf{g}^\downarrow \right\rangle = \mathbf{g}^\downarrow(\mathbf{r}, 0 | \Omega_i), \qquad (29)$$

$$\mathbf{A}\left\langle \xi^n \mathbf{g}^\downarrow \right\rangle = n\left\langle \xi^{n-1} \mathbf{g}^\downarrow \right\rangle, \qquad (30)$$

for $n \geq 1$, which can be solved recursively by starting with equation (29) for the zeroth moment and computing increasingly higher moments by using the previous moment on the right-hand side of equation (30). The stationary-flow fractions of phosphate and DOP that were last utilized in region Ω_i regardless of transit time are given from equations (11), (6), and (5) by $f_I^\downarrow = \left\langle g_I^\downarrow \right\rangle / P_I$ and $f_O^\downarrow = \left\langle g_O^\downarrow \right\rangle / P_O$.

[85] Computationally, we spatially discretize all fields on a grid of N grid points and organize the grid values of a given field into a column vector whose rows identify grid location $\mathbf{r}$. The partitioned phosphate and DOP fields, $g_I^\downarrow$ and $g_O^\downarrow$, thus become N-element column vectors so that $\mathbf{g}^\downarrow \equiv \left[g_I^\downarrow, g_O^\downarrow\right]^T$ is a $2N$-element column vector, and the linear differential operator $\mathbf{A}$ becomes a $2N \times 2N$ sparse matrix. The discretized equations (29) and (30) are therefore simple matrix equations, whose solution could be obtained by direct matrix inversion. In practice, an explicit inversion is avoided by an LU factorization of $\mathbf{A}$ followed by back-substitution. To ensure that $\mathbf{A}$ is in fact invertible, we add a term that restores the phosphate field to the known global average phosphate concentration with a very long timescale of 10^6 years. This constrains the global phosphate mass, thus removing a null space of $\mathbf{A}$ that is present without this constraint.

The "Out" Problem

[86] To compute the partitioned phosphate and DOP that will next be taken up on Ω_f, we use the adjoint Green function so that only one tracer field is necessary for each destination region Ω_f. The adjoint Green function $\mathbf{G}^{\dagger}(\mathbf{r}, \xi|\mathbf{r}') = \mathbf{G}^T(\mathbf{r}', -\xi|\mathbf{r})$ satisfies the initial value problem

$$(\partial_{\xi} + \mathbf{A}^{\dagger})\mathbf{G}^{\dagger}(\mathbf{r}, \xi|\mathbf{r}') = 0, \qquad (31)$$

with initial condition

$$\mathbf{G}^{\dagger}(\mathbf{r}, 0|\mathbf{r}') = \mathbf{I}\delta(\mathbf{r} - \mathbf{r}'). \qquad (32)$$

The fraction of nutrient and DOP at $\mathbf{r}$ that will next be taken up on Ω_f a time ξ later during $(\xi, \xi + d\xi)$ is given by $\widetilde{\boldsymbol{\mathcal{G}}}d\xi$, where $\widetilde{\boldsymbol{\mathcal{G}}} \equiv \left[\widetilde{\mathcal{G}}_I, \widetilde{\mathcal{G}}_O\right]^T$, which is related to $\mathbf{G}^{\dagger}(\mathbf{r}, \xi|\mathbf{r}')$ through equation (9) as

$$\widetilde{\boldsymbol{\mathcal{G}}}(\mathbf{r}, \xi|\Omega_f) = \int d^3r' \mathbf{G}^{\dagger}(\mathbf{r}, \xi|\mathbf{r}')\begin{bmatrix}\Omega_f(\mathbf{r}')\gamma(\mathbf{r}') \\ 0\end{bmatrix}, \qquad (33)$$

which satisfies

$$(\partial_{\xi} + \mathbf{A}^{\dagger})\widetilde{\boldsymbol{\mathcal{G}}}(\mathbf{r}, \xi|\Omega_f) = 0, \qquad (34)$$

with the initial condition

$$\widetilde{\boldsymbol{\mathcal{G}}}(\mathbf{r}, 0|\Omega_f) = \begin{bmatrix}\Omega_f(\mathbf{r})\gamma(\mathbf{r}) \\ 0\end{bmatrix}. \qquad (35)$$

For steady flow, the temporal moments $\left\langle \xi^n \widetilde{\boldsymbol{\mathcal{G}}} \right\rangle$ can again be obtained by recursing the following equations ($n \geq 1$):

$$\mathbf{A}^{\dagger}\left\langle \widetilde{\boldsymbol{\mathcal{G}}} \right\rangle = \widetilde{\boldsymbol{\mathcal{G}}}(\mathbf{r}, 0|\Omega_f), \qquad (36)$$

$$\mathbf{A}^{\dagger}\left\langle \xi^n \widetilde{\boldsymbol{\mathcal{G}}} \right\rangle = n\left\langle \xi^{n-1}\widetilde{\boldsymbol{\mathcal{G}}} \right\rangle. \qquad (37)$$

The stationary-flow fractions of phosphate and DOP that will next be taken up in region Ω_f regardless of transit time are given by equation (12) as $f_I^{\uparrow} = \left\langle \widetilde{\mathcal{G}}_I \right\rangle$ and $f_O^{\uparrow} = \left\langle \widetilde{\mathcal{G}}_O \right\rangle$.

[87] The adjoint here is most naturally defined with respect to a volume-weighted inner product. For the spatially discretized system, we therefore have that $\mathbf{A}^{\dagger} = \mathbf{W}^{-1}\mathbf{A}^T\mathbf{W}$, with $\mathbf{W} \equiv \mathbf{diag}([\mathbf{w}, \mathbf{w}])$, with $\mathbf{w}$ is the row vector of the grid-box volumes.

Appendix C: Uncertainty due to Phosphorus Cycling Parameters

[88] The uncertainties δZ in a quantity Z were estimated from the linear sensitivities to the phosphorus cycling model parameters b, σ, and κ evaluated in the base equilibrium state, that is as,

$$(\delta Z)^2 \equiv (\partial_b Z \delta b)^2 + (\partial_{\sigma} Z \delta \sigma)^2 + (\partial_{\kappa} Z \delta \kappa)^2 \qquad (38)$$

where we took $\delta b = 0.35$, $\delta \sigma = 0.15$, and $\delta \kappa = (0.25 \text{ year})^{-1}$ as reasonable rough uncertainties in the parameters themselves.

Appendix D: Connection Between Volume-Integrated Path Density and $\langle \mathcal{R} \rangle$

[89] Here we derive relationship (22) for export→uptake paths for which the necessary path density is $\bar{\eta} = \bar{\eta}_I + \bar{\eta}_O$, where $\bar{\eta}_I \equiv P_I f_I^{\downarrow} f_I^{\uparrow}$ is the phosphate path density defined by equation (15) and $\bar{\eta}_O \equiv P_O f_O^{\downarrow} f_O^{\uparrow}$ is the DOP path density. Substituting for the fractions $f_X^{\uparrow}$ and $f_X^{\downarrow}$ from equations (11), (12), (6), (5), and (9) we have

$$\int d^3r \ \bar{\eta}(\mathbf{r}, t) = \int d^3r \int_t^{\infty} dt_f \int_{-\infty}^t dt_i \int d^3r'' \int d^3r' \Omega_f(\mathbf{r}'', t_f)\gamma(\mathbf{r}'', t_f)$$
$$\times [G_{II}(\mathbf{r}'', t_f|\mathbf{r}, t)G_{IO}(\mathbf{r}, t|\mathbf{r}', t_i)$$
$$+ G_{IO}(\mathbf{r}'', t_f|\mathbf{r}, t)G_{OO}(\mathbf{r}, t|\mathbf{r}', t_i)]S(\mathbf{r}', t_i)\Omega_i(\mathbf{r}', t_i). \qquad (39)$$

[90] We now use the Chapman–Kolmogorov identity (sometimes also called the composition property) of Green functions, which for the 2×2 (PO$_4$, DOP) system states that

$$\int d^3r \ \mathbf{G}(\mathbf{r}'', t_f|\mathbf{r}, t)\mathbf{G}(\mathbf{r}, t|\mathbf{r}', t_i) = \mathbf{G}(\mathbf{r}'', t_f|\mathbf{r}', t_i). \qquad (40)$$

The (1,2) element of matrix equation (40) thus states that

$$\int d^3r [G_{II}(\mathbf{r}'', t_f|\mathbf{r}, t)G_{IO}(\mathbf{r}, t|\mathbf{r}', t_i) \qquad (41)$$
$$+ G_{IO}(\mathbf{r}'', t_f|\mathbf{r}, t)G_{OO}(\mathbf{r}, t|\mathbf{r}', t_i)] = G_{IO}(\mathbf{r}'', t_f|\mathbf{r}', t_i).$$

Applying equation (41) to equation (39) to perform the d^3r integral over intermediate transit points, we have

$$\int d^3r \ \bar{\eta}(\mathbf{r}, t) = \int_t^{\infty} dt_f \int_{-\infty}^t dt_i \int d^3r'' \int d^3r' \ \Omega_f(\mathbf{r}'', t_f)\gamma(\mathbf{r}'', t_f)$$
$$\times G_{IO}(\mathbf{r}'', t_f|\mathbf{r}', t_i)S(\mathbf{r}', t_i)\Omega_i(\mathbf{r}', t_i)$$
$$= \int_t^{\infty} dt_f \int_{-\infty}^t dt_i \int d^3r'' \ \Omega_f(\mathbf{r}'', t_f)\gamma(\mathbf{r}'', t_f)$$
$$\times g_I^{\downarrow}(\mathbf{r}'', t_f|\Omega_i, t_i), \qquad (42)$$

where the last equality follows from the definition (5) for the partitioned phosphate $g_I^{\downarrow}$.

[91] We now specialize to stationary flow so that

$$\int d^3r'' \ \Omega_f(\mathbf{r}'', t_f)\gamma(\mathbf{r}'', t_f)g_I^{\downarrow}(\mathbf{r}'', t_f|\Omega_i, t_i)$$
$$= \int d^3r'' \ \Omega_f(\mathbf{r}'')\gamma(\mathbf{r}'')g_I^{\downarrow}(\mathbf{r}'', t_f - t_i|\Omega_i) \qquad (43)$$
$$\equiv \mathcal{J}(t_f - t_i, \Omega_i \rightarrow \Omega_f),$$

where the last definition is just equation (17). Thus, choosing $t = 0$ without loss of generality because t is arbitrary for stationary flow, we have

$$\int d^3r \ \bar{\eta}(\mathbf{r}) = \int_{-\infty}^0 dt_i \int_0^{\infty} dt_f \mathcal{J}(t_f - t_i, \Omega_i \rightarrow \Omega_f). \qquad (44)$$

Now changing variables from t_f to $\tau = t_f - t_i$ we have

$$\int d^3r \ \bar{\eta}(\mathbf{r}) = \int_{-\infty}^0 dt_i \int_{-t_i}^{\infty} d\tau \ \mathcal{J}(\tau, \Omega_i \rightarrow \Omega_f), \qquad (45)$$

and changing the order of integration gives

$$\int d^3r \ \bar{\eta}(\mathbf{r}) = \int_0^\infty d\tau \int_{-\tau}^0 dt_i \ \mathcal{J}(\tau, \Omega_i \to \Omega_f)$$

$$= \int_0^\infty d\tau \ \tau \ \mathcal{J}(\tau, \Omega_i \to \Omega_f) \equiv \langle \mathcal{R} \rangle. \quad (46)$$

Thus, for the exp→upt paths, we have

$$\langle \mathcal{R} \rangle = \int d^3r \ (\bar{\eta}_I + \bar{\eta}_O). \quad (47)$$

As discussed in the main text, $\bar{\eta}_O$ can be neglected in equation (47) to an excellent approximation.

Appendix E: The Nature of the Flux-Density Distribution $\mathcal{J}$

[92] The timescales provided by the mean age on exit, Γ, and the mean residence time, $\bar{\tau}$, are moments of the distributions $\mathcal{J}$ and $\mathcal{R} = \tau \mathcal{J}$, which typically have long tails. Thus, while Γ and $\bar{\tau}$ are a very useful quantitative summary of these distributions, they tend to be much longer than the most probable transit times (also called modes) at which these distributions are peaked. To contrast the modes with the means, and to more fully characterize the times with which phosphorus is cycled in the ocean, we briefly examine the flux-density distribution, $\mathcal{J}$, for transport from the SANTZ to the two North-Atlantic receptor regions in the data-assimilated equilibrium state.

[93] Figure 13 shows $\mathcal{J}$ as a function of transit time for the three path types considered (pre→srf, exp→srf, exp→upt). The mode lies between ~30 and 50 years (shorter for the SubTroNA than for the more distant SubPlrNA). The pre→srf and exp→srf distributions are very similar, indicating that both preformed and regenerated nutrients are transported to these receptor regions by similar thermocline paths. The exp→srf distribution decays more slowly because the SANTZ particle export accesses some deeper paths compared to the preformed case. The exp→upt distribution has the longest mode and slowest decay because of the extra time required to "find" the uptaking organisms. All distributions
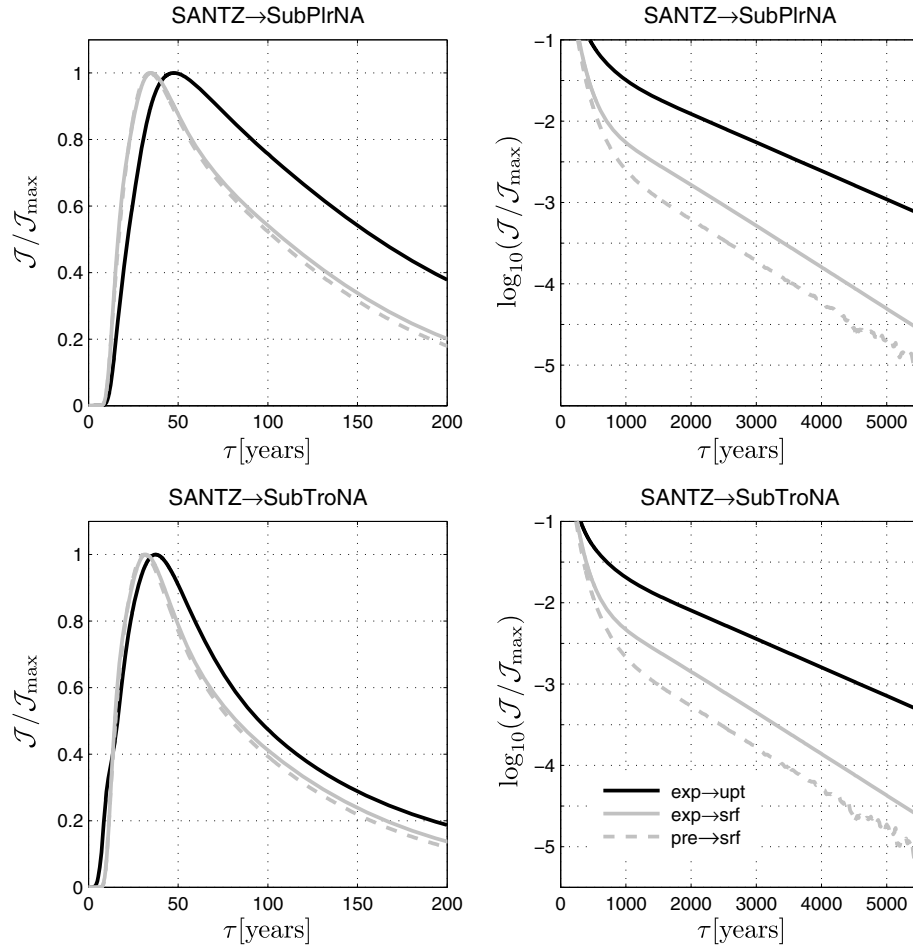

Figure 13. The three types of flux-density distributions $\mathcal{J}$ for transport from the SANTZ to the subpolar and subtropical North Atlantic (SubPlrNA and SubTroNA) as a function of transit time τ. For plotting convenience, the distributions are normalized to their peak value, $\mathcal{J}_{\max}$. As indicated in the legend, the distributions are for the transport of SANTZ preformed nutrients to their exit back into euphotic surface layer of the destination region (pre→srf), for the transport of nutrients last utilized in the SANTZ and then regenerated to their exit back into surface layer (exp→srf), and for the transport of nutrients last utilized in the SANTZ to their next biological uptake (exp→upt). The plots on the right show $\log_{10}(\mathcal{J}/\mathcal{J}_{\max})$ for $\tau > 50$ years to highlight the asymptotic exponential decay.

are skewed with long tails, so that their first moment, Γ, is much longer than their mode. Table 1 shows that, as expected, the slower the decay, the larger Γ: very roughly $\Gamma \sim 100$, 200, and 500 years for pre→srf, exp→srf, and exp→upt, respectively, several times to an order of magnitude longer than the most probable transit times.

[94] The logarithmic scale in Figure 13 reveals exponential asymptotic decay for $\tau > 1500$ years. This is the signature of the longest-lived eigenmode of equation (1). The decay e-folding time is therefore independent of receptor region and depends only on the boundary conditions to which equation (1) is subjected. Because regenerated and preformed nutrients obey the same homogeneous boundary condition of zero concentration in the euphotic zone, both the pre→srf and exp→srf distributions decay with the same e-folding time, which has a value of 860 years. The partitioned nutrients $g_I^{\downarrow}$, whose uptake rate gives the exp→upt $\mathcal{J}$, are relaxed to zero (that is, taken up biologically) with the finite, inhomogeneous rate-constant field $\gamma(\mathbf{r})$ and hence have a longer eigenmode e-folding time of 1240 years.

References

Boyd, P. W., et al. (2007), Mesoscale iron enrichment experiments 1993-2005: Synthesis and future directions, *Science*, *315*, 612–617.

DeVries, T., and F. Primeau (2009), Atmospheric pCO2 sensitivity to the solubility pump: Role of the low-latitude ocean, *Global Biogeochem. Cycles*, *23*, doi:10.1029/2009GB003537.

DeVries, T., and F. Primeau (2011), Dynamically and observationally constrained estimates of water-mass distributions and ages in the global ocean, *J. Phys. Oceanogr.*, *41*, 2381–2401.

Ganachaud, A., and C. Wunsch (2002), Oceanic nutrient and oxygen transports and bounds on export production during the World Ocean Circulation Experiment, *Global Biogeochem. Cycles*, *16*, 1057.

Gnanadesikan, A., J. P. Dunne, R. M. Key, K. Matsumoto, J. L. Sarmiento, R. D. Slater, and P. S. Swathi (2004), Oceanic ventilation and biogeochemical cycling: Understanding the physical mechanisms that produce realistic distributions of tracers and productivity, *Global Biogeochem. Cycles*, *18*, doi:10.1029/2003GB00209.

Gnanadesikan, A., R. D. Slater, N. Gruber, and J. L. Sarmiento (2002), Oceanic vertical exchange and new production: A comparison between models and observations, *Deep Sea Res., Part II*, *49*, 363–401.

Guo, X., X.-H. Zhu, Q.-S. Wu, and D. Huang (2012), The Kuroshio nutrient stream and its temporal variation in the East China Sea, *J. Geophys. Res.*, *117*, doi:10.1029/2011JC007292.

Hall, T. M., and M. Holzer (2003), Advective-diffusive mass flux and implications for stratosphere-troposphere exchange, *Geophys. Res. Lett.*, *30*, 1222.

Hansell, D. A., C. A. Carlson, and R. Schlitzer (2012), Net removal of major marine dissolved organic carbon fractions in the subsurface ocean, *Global Biogeochem. Cycles*, *26*, 263–266.

Holzer, M. (2009), The path density of interhemispheric surface-to-surface transport. Part I: Development of the diagnostic and illustration with an analytic model, *J. Atmos. Sci.*, *66*, 2159–2171.

Holzer, M., and T. M. Hall (2000), Transit-time and tracer-age distributions in geophysical flows, *J. Atmos. Sci.*, *57*, 3539–3558.

Holzer, M., and T. M. Hall (2008), Tropospheric transport climate partitioned by surface origin and transit time, *J. Geophys. Res.*, *113*, doi:10.1029/2007JD009115.

Holzer, M., and F. W. Primeau (2006), The diffusive ocean conveyor, *Geophys. Res. Lett.*, *33*, doi:10.1029/2006GL026232.

Holzer, M., and F. W. Primeau (2008), The path-density distribution of oceanic surface-to-surface transport, *J. Geophys. Res.*, *113*, doi:10.1029/2006JC003976.

Holzer, M., C. Orbe, and F. W. Primeau (2012), Stratospheric mean residence time and mean age at the tropopause: Connections and implications for observational constraints, *J. Geophys. Res.*, *117*, doi:10.1029/2012JD017547.

Jenkins, W. J. (1982), Oxygen utilization rates in North Atlantic subtropical gyre and primary production in oligotrophic systems, *Nature*, *300*, 246–248.

Jenkins, W. J., and S. C. Doney (2003), The subtropical nutrient spiral, *Global Biogeochem. Cycles*, *17*, 1110.

Khatiwala, S., F. Primeau, and M. Holzer (2012), Ventilation of the deep ocean constrained with tracer observations and implications for radiocarbon estimates of ideal mean age, *Earth Planet. Sci. Lett.*, *325-326*, 116–125.

Krémeur, A.-S., M. Lévy, O. Aumont, and G. Reverdin (2009), Impact of the subtropical mode water biogeochemical properties on primary production in the North Atlantic: New insights from an idealized model study, *J. Geophys. Res.*, *114*, 141–149.

Marinov, I., A. Gnanadesikan, J. L. Sarmiento, J. R. Toggweiler, M. Follows, and B. K. Mignone (2008), Impact of oceanic circulation on biological carbon storage in the ocean and atmospheric pCO2, *Global Biogeochem. Cycles*, *22*, doi:10.1029/2007GB002958.

Marinov, I., A. Gnanadesikan, J. R. Toggweiler, and J. L. Sarmiento (2006), The Southern Ocean biogeochemical divide, *Nature*, *441*, 964–967.

Martin, J. W., G. A. Knauer, D. M. Karl, and W. W. Broenkow (1987), VERTEX: Carbon cycling in the NE Pacific, *Deep Sea Res.*, *34*, 267–285.

McGillicuddy, D. J., L. A. Anderson, S. C. Doney, and M. E. Maltrud (2003), Eddy-driven sources and sinks of nutrients in the upper ocean: Results from a 0.1° resolution model of the North Atlantic, *Global Biogeochem. Cycles*, *17*, 1035.

Najjar, R. G., J. L. Sarmiento, and J. R. Toggweiler (1992), Downward transport and fate of organic matter in the ocean: Simulations with a general circulation model, *Global Biogeochem. Cycles*, *6*, 45–76.

Orbe, C., M. Holzer, and L. M. Polvani (2012), Flux distributions as robust diagnostics of stratosphere-troposphere exchange, *J. Geophys. Res.*, *117*, doi:10.1029/2011JD016455.

Oschlies, A., W. Koeve, W. Rickels, and K. Rehdanz (2010), Side effects and accounting aspects of hypothetical large-scale Southern Ocean iron fertilization, *Biogeosciences*, *7*, 4017–4035.

Palter, J. B., and M. S. Lozier (2008), On the source of Gulf Stream nutrients, *J. Geophys. Res.*, *113*, doi:10.1029/2007JC004611.

Palter, J. B., M. S. Lozier, and R. T. Barber (2005), The effect of advection on the nutrient reservoir in the North Atlantic subtropical gyre, *Nature*, *437*, doi:10.1038/nature03969.

Palter, J. B., J. L. Sarmiento, A. Gnanadesikan, J. Simeon, and R. D. Slater (2010), Fueling export production: nutrient return pathways from the deep ocean and their dependence on the Meridional Overturning Circulation, *Biogeosciences*, *7*, 3549–3568.

Pelegrí, J. L., and G. T. Csanady (1991), Nutrient transport and mixing in the Gulf Stream, *J. Geophys. Res.*, *96*, 2577–2583.

Pelegrí, J. L., G. T. Csanady, and A. Martins (1996), The North Atlantic nutrient stream, *J. Oceanogr.*, *52*, 275–299.

Primeau, F. W. (2005), Characterizing transport between the surface mixed layer and the ocean interior with a forward and adjoint global ocean transport model, *J. Phys. Oceanogr.*, *35*, 545–564.

Primeau, F. W., and M. Holzer (2006), The ocean's memory of the atmosphere: Residence-time and ventilation-rate distributions of water masses, *J. Phys. Oceanogr.*, *36*, 1439–1456.

Sarmiento, J. L., N. Gruber, M. A. Brzezinski, and J. P. Dunne (2004), High-latitude controls of thermocline nutrients and low latitude biological productivity, *Nature*, *427*, 56–60.

Schlitzer, R. (2002), Carbon export fluxes in the Southern Ocean: results from inverse modeling and comparison with satellite based estimates, *Deep Sea Res., Part II*, *49*, 1623–1644.

Trenberth, K. E., W. G. Large, and J. G. Olson (1989), A global ocean wind stress climatology based on ECMWF analyses, *Tech. Rep. TN-3381STR*, National Center for Atmospheric Research.

Williams, R. G., V. Roussenov, and M. J. Follows (2006), Nutrient streams and their induction into the mixed layer, *Global Biogeochem. Cycles*, *20*, doi:10.1029/2005GB00258.

Williams, R. G., E. McDonagh, V. M. Roussenov, S. Torres-Valdess, B. King, R. Sanders, and D. A. Hansell (2011), Nutrient streams in the North Atlantic: Advective pathways of inorganic and dissolved organic nutrients, *Global Biogeochem. Cycles*, *25*, doi:10.1029/2010GB003853.